A&A 650, A57 (2021)
https://doi.org/10.1051/0004-6361/202140297

Astronomy & Astrophysics

The properties of the AGN torus as revealed from a set of unbiased *NuSTAR* observations

X. Zhao[1,2], S. Marchesi[3,1], M. Ajello[1], D. Cole[1], Z. Hu[1], R. Silver[1], and N. Torres-Albà[1]

[1] Department of Physics & Astronomy, Clemson University, Clemson, SC 29634, USA
e-mail: xiuruiz@clemson.edu
[2] Harvard-Smithsonian Center for Astrophysics, 60 Garden Street, Cambridge, MA 02138, USA
[3] INAF-Osservatorio Astronomico di Bologna, Via Piero Gobetti, 93/3, 40129 Bologna, Italy

Received 7 January 2021 / Accepted 30 March 2021

ABSTRACT

The obscuration observed in active galactic nuclei (AGNs) is mainly caused by dust and gas distributed in a torus-like structure surrounding the supermassive black hole. However, the properties of the obscuring torus of an AGN in X-ray have not yet been fully investigated because of a lack of high-quality data and proper models. In this work, we perform a broadband X-ray spectral analysis of a large, unbiased sample of obscured AGNs (with line-of-sight column density $23 \leq \log(N_{\rm H}) \leq 24$) in the nearby Universe for which high-quality archival *NuSTAR* data are available. We analyzed the source spectra using the recently developed `borus02` model, which enables us to accurately characterize the physical and geometrical properties of AGN-obscuring tori. We compare our results obtained from the unbiased Compton-thin AGNs with those of Compton-thick AGNs. We find that Compton-thin and Compton-thick AGNs may possess similar tori, whose average column density is Compton thick ($N_{\rm H,tor,ave} \approx 1.4 \times 10^{24}$ cm^{-2}), but they are observed through different (under-dense or over-dense) regions of the tori. We also find that the obscuring torus medium is significantly inhomogeneous, with the torus average column densities being significantly different from their line-of-sight column densities (for most of the sources in the sample). The average torus covering factor of sources in our unbiased sample is $c_{\rm f} = 0.67$, suggesting that the fraction of unobscured AGNs is ∼33%. We developed a new method to measure the intrinsic line-of-sight column density distribution of AGNs in the nearby Universe, and find the results to be in good agreement with constraints from recent population synthesis models.

Key words. galaxies: active – Galaxy: nucleus – X-rays: galaxies

1. Introduction

Active galactic nuclei (AGNs) are some of the most powerful objects in the sky because of the extreme accretion process of the super-massive black holes (SMBHs) in the center of galaxies (Soltan 1982; Richstone et al. 1998). The material (gas and dust) surrounding the SMBH not only feeds the central monster but is the origin of the obscuration of the AGN (see Hickox & Alexander 2018, for a recent review). Studying the properties of this obscuring material in AGNs is key to understanding the growth of SMBHs. The AGN unified model (Antonucci 1993; Urry & Padovani 1995) suggests that the obscuring material in the AGNs is shaped as an optically thick torus-like structure. The obscuring torus was initially thought to be smooth. However, many recent observations show that the material within the torus is clumpy rather than uniformly distributed (see Netzer 2015, for a recent review). For example, the rapid variable sources and eclipse events found in X-ray observations (e.g., Risaliti et al. 2002; Markowitz et al. 2014; Laha et al. 2020) and the observed 10 μm silicate features in the infrared (IR) spectra cannot be explained by a smooth torus (e.g., Nenkova et al. 2002; Mason et al. 2009).

Based on the obscuration of the torus, AGNs can be categorized into unobscured when the column density along the line of sight is $N_{\rm H,los} < 10^{22}$ cm^{-2}, and obscured when $N_{\rm H,los} > 10^{22}$ cm^{-2}. The most obscured sources are called Compton thick (CT-) AGNs when $N_{\rm H,los} > 10^{24}$ cm^{-2}. Moreover, AGNs with different levels of obscuration are the main contributors to the cosmic X-ray background (CXB; the diffuse X-ray emission in the universe; e.g., Maccacaro 1991; Madau et al. 1994; Comastri et al. 1995). Hard X-ray surveys are more efficient in detecting obscured AGNs because high-energy photons can more easily penetrate the dense material surrounding the SMBH. However, only a small number of CT-AGNs have been discovered so far (e.g., Risaliti et al. 1999; Burlon et al. 2011; Ricci et al. 2015; Lanzuisi et al. 2018) because of their large obscuration, which makes it difficult to both detect them and properly measure their column density. Consequently, the uncertainties on the measurement of the intrinsic distribution of the column density of AGNs are still significant. The fraction of CT-AGNs predicted by AGN population synthesis models (∼30–50%; Gilli et al. 2007; Ueda et al. 2014; Buchner et al. 2015; Ananna et al. 2019) is much higher than what has been observed so far (∼10–30%; Burlon et al. 2011; Ricci et al. 2015; Lansbury et al. 2017; Masini et al. 2018; Zappacosta et al. 2018). Therefore, the intrinsic column density distribution of AGNs is still controversial.

In this work, we perform a broadband X-ray spectral analysis of high-quality (soft and hard) data available for a large, unbiased sample of obscured AGNs in the local universe ($z < 0.15$). In Sect. 2, we introduce the criteria that are used to select the unbiased AGN sample and describe the X-ray spectral analysis technique. In Sect. 3, we report the spectral analysis results. In Sect. 4, we develop a new method to calculate the intrinsic line-of-sight column density distribution of the AGNs in the local Universe. We also compare our derived

distribution with the results obtained in previous observations and the constraints from different population synthesis models. All reported uncertainties are at 90% confidence level unless otherwise stated. Standard cosmological parameters are adopted as follows: $\langle H_0 \rangle = 70\,\mathrm{km\,s^{-1}\,Mpc^{-1}}$, $\langle q_0 \rangle = 0.0$, and $\langle \Omega_\Lambda \rangle = 0.73$.

2. Sample selection and spectral analysis

2.1. Selection criteria

The sources presented in this work are selected from the 100-month Palermo *Swift*-BAT catalog[1] (Marchesi et al., in prep.), which covers 50% of the sky at the 15–150 keV flux limit of $\sim 5.4\times10^{-12}$ erg cm^{-2} s^{-1}. The selection criteria are as follows:

1. Sources with line-of-sight column density[2] ($N_{\rm H,los}$) between 10^{23} and 10^{24} cm^{-2}. To characterize the physical and geometrical properties of the obscuring material around the SMBH, a clear signal is needed from the reprocessed component of the obscuring torus to overcome the line-of-sight component. Though ideal for studying the obscuring torus, when sampling, there is significant bias against CT-AGNs. Therefore, here we select heavily obscured Compton-thin AGNs, against which there is less bias when studying the obscuring torus. In sources with $N_{\rm H,los} < 10^{23}$ cm^{-2}, the contribution of the reprocessed component to the overall AGN emission is negligible (<5% at 2–10 keV; Baloković et al. 2018), which makes the derivation of the torus properties a difficult process in those sources. We therefore select Compton-thin sources with $N_{\rm H,los} > 10^{23}$ cm^{-2} in our study of the AGN torus. We analyzed the nearby CT-AGNs selected from the *Swift*-BAT catalog in a separate set of papers (Marchesi et al. 2018, 2019, and in prep., Zhao et al. 2019a,b).
2. Available *NuSTAR* data. *NuSTAR* data are instrumental in properly characterizing the properties of heavily obscured AGNs in the local universe because of the significant suppression of their spectra at soft X-rays (see, e.g., Civano et al. 2015; Marchesi et al. 2018).

The obscuring material that reprocesses the X-ray emissions from the "hot corona" is mainly related to the dusty torus (<10 pc) proposed by the AGN unified model and to the interstellar medium (ISM; >kpc) of the host galaxy (see, Netzer 2015; Almeida & Ricci 2017; Hickox & Alexander 2018, for recent reviews). The typical column density $N_{\rm H}$ toward the nucleus decreases with size scale as R^{-2} (where R is the distance from the central SMBH). Thus, the $N_{\rm H}$ from the galaxy-wide scale is thought to be $N_{\rm H} < 10^{23}$ cm^{-2}, except for galaxy mergers (e.g., Di Matteo et al. 2005) and high-redshift quasars where the galaxies are rich in gas (Circosta et al. 2019). The dusty gas in the compact torus can produce obscuration up to $N_{\rm H} \approx 10^{25}$ cm^{-2}. Our selected sources are heavily obscured ($N_{\rm H} > 10^{23}$ cm^{-2}) and are in the local Universe ($z < 0.15$), and no evidence has been found for merger events. Therefore, we assume that the obscuring material that reprocesses the X-ray emission in our sources is mainly from the AGN torus.

A total of 93 out of ~1000 AGNs in the BAT catalog have been selected and analyzed in this work. The information about the observations used when analyzing each source is listed in the Appendix. The median redshift of the sources in our finalized sample is $\langle z \rangle = 0.02776$ (i.e., the median distance is $\langle d \rangle \sim 122$ Mpc).

2.2. Spectral analysis

We perform a broadband (1–78 keV) X-ray spectral analysis of all 93 sources in our sample. *NuSTAR* (3–78 keV) data provide coverage in the hard X-rays. For the soft-X-ray band, we use archival *XMM-Newton* data when they are available (1–10 keV; 48 sources); otherwise we use archival *Chandra* data (1–7 keV; 19 sources). We use *Swift*-XRT data (1–10 keV; 26 sources) when neither *XMM-Newton* nor *Chandra* data are available. The details of the data reduction are listed and described in Appendix A.

The spectra are fitted using `XSPEC` (Arnaud 1996) version 12.10.0c. The photoelectric cross-section is from Verner et al. (1996); the element abundance is from Anders & Grevesse (1989) and metal abundance is fixed to solar; the Galactic absorption column density is obtained using the `nh` task (Kalberla et al. 2005) in `HEAsoft` for each source. The χ^2 statistic is adopted when *XMM-Newton* data and *Chandra* data are used, while the C statistic (Cash 1979) is used when *Swift*-XRT data are applied due to the low quality of the *Swift*-XRT spectra and the limited number of counts in each bin.

The spectra of heavily obscured AGNs are complicated by the emergence of the reprocessed component, including the Compton scattering and fluorescent emission lines, which are buried by the line-of-sight component in the unobscured AGN spectra. However, despite the additional difficulty of characterizing the spectra, this reprocessed component becomes a perfect tool to estimate the physical and geometrical properties of the obscuring material surrounding the central SMBH. In this work, following Zhao et al. (2020), we analyze the spectra of the sources in our sample using the self-consistent Borus model (Baloković et al. 2018), which optimizes the exploration of the parameter space and has been intensively used to characterize heavily obscured AGNs.

The complete Borus model used in the spectral analysis consists of three components:

(A) A reprocessed component produced by the obscuring material near the SMBH, including the Compton-scattered continuum and fluorescent lines, characterized by `borus02`. `borus02` assumes a sphere with conical cutouts at both poles (Baloković et al. 2018), approximating a torus with an opening angle that can vary in the range of $\theta_{\rm Tor} = [0{-}84]^\circ$, corresponding to a torus covering factor of $c_{\rm f} = \cos(\theta_{\rm Tor}) = [1{-}0.1]$. The inclination angle, which is the angle between the axis of the AGN and the observer's line of sight, is also a free parameter ranging from $\theta_{\rm inc} = [18{-}87]^\circ$, where $\theta_{\rm obs} = 18^\circ$ is when the AGN is observed face-on and $\theta_{\rm obs} = 87^\circ$ is observed edge-on. The average column density of the obscuring torus can vary in the range of $\log(N_{\rm H,tor}) = [22.0{-}25.5]$.

(B) A line-of-sight component or the absorbed intrinsic continuum, described by a cut-off power law, denoted by `cutoffpl` in `XSPEC`, multiplied by an obscuring component, including both the photoelectric absorption (`zphabs`) and the Compton-scattering (`cabs`) effects. It is worth noting that the torus column density in the reprocessed component is decoupled from the line-of-sight column density: the torus column density is an average property of the obscuring torus. In contrast, the line-of-sight column density represents a quantity that is along our line of sight and could vary when observed at different epochs.

[1] http://bat.ifc.inaf.it/100m_bat_catalog/100m_bat_catalog_v0.0.htm

[2] For sources also detected in the BAT 70-month catalog, we use the spectral properties measured in Ricci et al. (2017a). We measured their spectral properties using the *Swift*-BAT data and soft X-ray data for the rest of the sources.

The line-of-sight column density $N_{\rm H,los}$ can be significantly different from $N_{\rm H,tor}$, which can be used as an approximation of the nonuniform (clumpy) distribution of matter surrounding the SMBH (see discussion in Sect. 4.2 of Baloković et al. 2018). Buchner et al. (2019), Tanimoto et al. (2019), who assume a clumpy torus scenario, provide a more realistic description of the obscuring material surrounding the accreting SMBH. However, these authors do not provide information about the global average properties of the torus, such as for example its average column density, which is a significant focus of this paper. Moreover, the Tanimoto et al. (2019) model has not yet been made publicly available.

(C) A scattered component modeling the fractional AGN emission that is scattered rather than absorbed by the obscuring material. The scattered component is characterized by an unabsorbed cut-off power law multiplied by a constant. The fractional unabsorbed continuum is usually less than 5–10% of the intrinsic continuum (see, e.g., Noguchi et al. 2010; Marchesi et al. 2016) and accounts for the AGN emission at low-energy below a few keV.

In the process of modeling the spectra, we tie the photon indices, Γ, the cut-off energy, $E_{\rm cut}$, and the normalization, norm, of the intrinsic continuum, the reprocessed component, and the fractional unabsorbed continuum together, assuming that the three components have the same origin. The photon index in `borus02` ranges in [1.4–2.6], and therefore the photon index in the cut-off power law varies between 1.4 and 2.6 as well.

The Borus model is used in the following `XSPEC` configuration:

$$\begin{aligned}&\text{Model} = \text{constant}_1 * \text{phabs} * (\text{borus02+}\\&\text{zphabs} * \text{cabs} * \text{cutoffpl} + \text{constant}_2 * \text{cutoffpl}),\end{aligned} \quad (1)$$

where $\texttt{constant}_1$ is the cross-calibration between *NuSTAR* and the soft-X-ray observatories, that is, *XMM-Newton*, *Chandra*, and *Swift*-XRT; `phabs` models the Galactic absorption from our Galaxy; and $\texttt{constant}_2$ is the fraction of the unabsorbed continuum in the scattered component.

The cut-off energy is fixed at $E_{\rm cut} = 500$ keV for all sources, except for ESO 383-18, whose cut-off energy is found to be $E_{\rm cut} < 20$ keV. The spectra of nine sources (ESO 263-13, Mrk 3, NGC 835, NGC 2655, NGC 4102, NGC 4258, NGC 4507, NGC 5728 and NGC 7319) all show strong nonAGN thermal emission around 1 keV, which may be caused by the star formation process and/or diffuse gas emission. We use `mekal` (Mewe et al. 1985) to model this nonAGN thermal contribution: the temperature and the relative metal abundance in `mekal` are both left free to vary. To better constrain the parameters of the `mekal` model, we fit the spectra of these sources down to 0.3 keV. When analyzing the spectra of 3C 445, we add a few Gaussian lines to model different emission lines. The relative iron abundance of the reprocessed component, $A_{\rm Fe}$, is fixed to 1 (the solar value), except for three sources (3C 445, 3C 452 and ESO 383-18), where a significant improvement in spectral fit ($>3\sigma$ using `ftest` in `XSPEC`) has been found when $A_{\rm Fe}$ is free to vary. The best-fit iron abundances are $A_{\rm Fe,3C\,445} = 0.32^{+0.05}_{-0.08}$, $A_{\rm Fe,3C\,452} = 0.41^{+0.05}_{-0.05}$, and $A_{\rm Fe,ESO\,383-18} = 0.19^{+0.07}_{-0.05}$.

We note that the obscuring material in the AGNs might also originate from the polar dust outflow as revealed by IR observations (e.g., Tristram et al. 2007). However, the X-ray observations are less affected by the polar outflow because the gas density in the polar outflow is much less than that in the torus (Wada et al. 2016). Indeed, the covering factors measured in X-ray are systematically smaller than those measured in IR (see, Fig. 2 in Tanimoto et al. 2019). This suggests that the typical size of the X-ray obscuring material is much smaller (i.e., the torus) than the typical sizes of the IR emission (i.e., torus + polar dust). Therefore, in the following discussion, we assume that absorption measured in the X-ray spectra of the sources in our sample is mainly due to the obscuring material in the torus, except for a few cases discussed in Sect. 3.

3. Results

The spectra of 93 sources and their best-fit models can be found online[3]. The best-fit results of the spectral analysis, that is, line-of-sight column density, $N_{\rm H,los}$, torus average column density, $N_{\rm H,tor}$, cosine of the inclination angle, $\cos(\theta_{\rm inc})$, torus covering factors, $c_{\rm f}$, 2–10 keV flux, $\rm Flux_{2-10}$, and 2–10 keV intrinsic (absorption-corrected) luminosity, $L_{\rm int,2-10}$, are reported in Tables A.2–A.4 when *XMM-Newton*, *Chandra*, and *Swift*-XRT data are used, respectively. For 15 sources in our sample, the contributions of their reprocessed emission to the overall spectra are marginal, such that the parameters of the reprocessed component, for example the torus average column density, inclination angle, and torus covering factor, cannot be constrained at all. Therefore we analyze their spectra using only the line-of-sight component and the scattered component for those sources. Eight sources in our sample are found to have line-of-sight column density $N_{\rm H,los} < 10^{23}\,{\rm cm^{-2}}$ or $N_{\rm H,los} > 10^{24}\,{\rm cm^{-2}}$, and therefore these sources are excluded from our sample. The spectra and best-fit model predictions of four representative sources have been plotted in Fig. A.1.

Flux variations are commonly found in the X-ray spectra of AGNs, especially when multiple observations are taken over timescales that vary from weeks to years (e.g., Guainazzi 2002; Risaliti 2002; Markowitz et al. 2014). Such variabilities are commonly explained by either the fluctuation of the AGN intrinsic emission (e.g., Nandra 2001) or the variation in the absorbing column density along the line of sight (see, e.g., Risaliti et al. 2002; Bianchi et al. 2012). Within the 93 sources in our sample, 20 sources are semi-simultaneously observed by *NuSTAR* and the soft-X-ray observatories. In the remaining 73 sources, 43 (~59%) are measured with significant flux variations between the soft- and hard-X-ray observations (2–10 keV flux variation >20 percent). Within these 43 sources, 16 mainly show intrinsic emission variation; 15 sources show $N_{\rm H,los}$ variation; and the flux variabilities of 12 sources can be explained only by considering both intrinsic emission and $N_{\rm H,los}$ variations. The details of the variability analysis are reported in Appendix B. The best-fit results of the sources with flux variability are summarized in Table B.1. It is worth noting that if a source had multiple soft-X-ray observations, we chose the one taken closest to their *NuSTAR* observation time. Therefore, the fraction of the sources in our sample that experienced flux variabilities might be even higher if all soft-X-ray observations are taken into account; however, we cannot exclude the possibility that the $N_{\rm H,los}$ measured with different instruments may have different values (apparent variability) due to different bandpasses, energy resolution, and effective areas. The $N_{\rm H,los}$ reported in Tables A.2–A.4 are those measured in the *NuSTAR* observing epoch, and we use them in the following discussions.

Marchesi et al. (2019, hereafter M19) reported the CT-AGNs in the nearby Universe, which are also selected from the BAT 100-month catalog and are covered by *NuSTAR* data. The sources were analyzed using the `borus02` model as well, with the distinction that the inclination angle is fixed in the

[3] https://science.clemson.edu/ctagn/project/

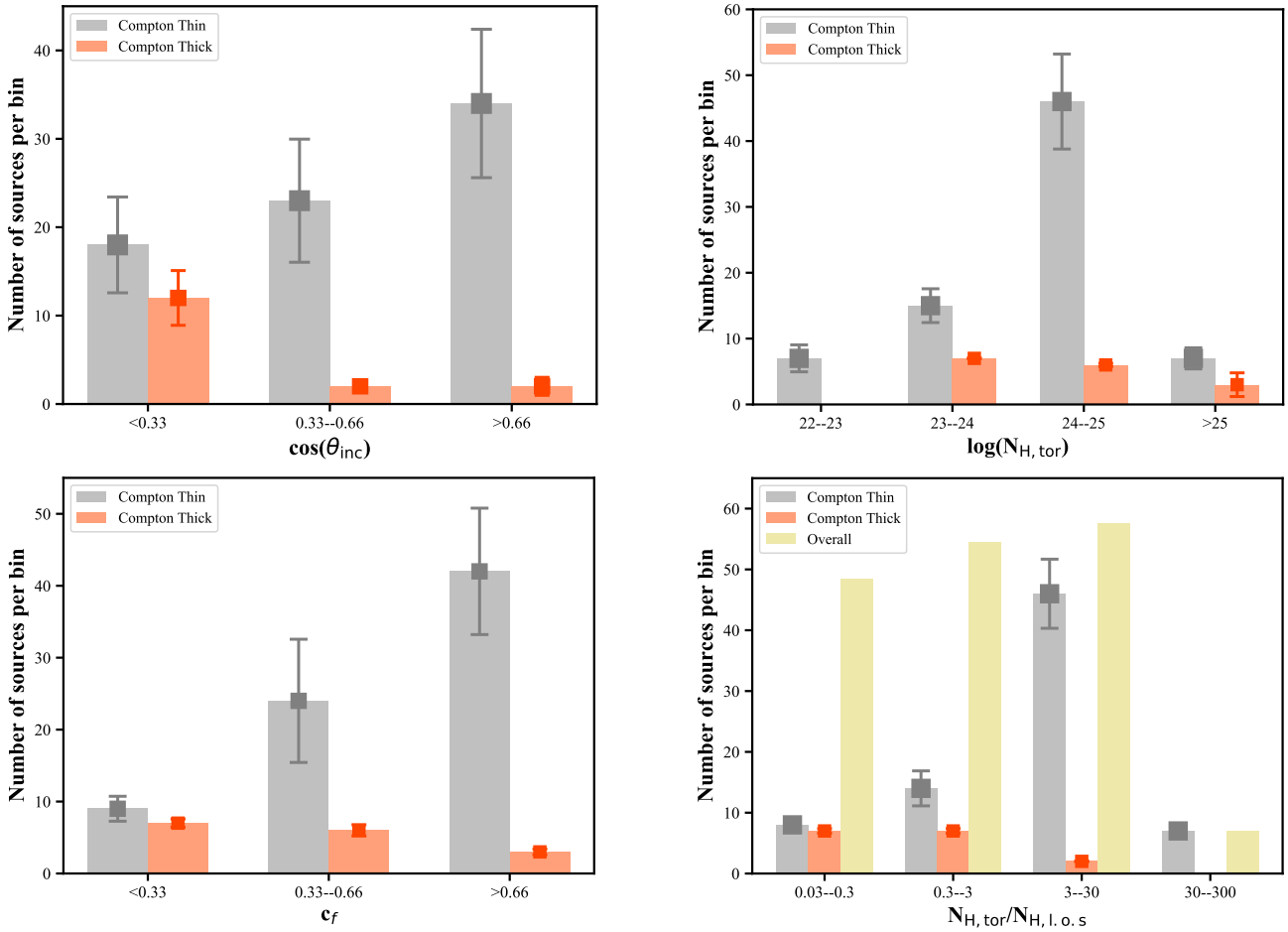

Fig. 1. *Left to right* in the *first row and second row*: number of sources with a specific range of inclination angles, $\cos(\theta_{\rm inc})$, torus column densities, $\log(N_{\rm H,tor})$, torus covering factors, $c_{\rm f}$, and torus column density contrast ratios, $N_{\rm H,tor}/N_{\rm H,los}$, from the Compton-thin sources in our sample (gray histogram) and CT sources from M19 (orange histogram), respectively. $\cos(\theta_{\rm inc}) \sim 0.05$ is when the AGN is observed edge-on and $cos(\theta_{\rm inc}) \sim 0.95$ is when the AGN is observed face-on. The error bar is at 90% confidence level. The overall distribution of the torus column density contrast ratio after rescaling is plotted in yellow. We do not include the 15 sources fitted with only a line-of-sight component and a scattered component here.

edge-on direction when fitting the spectra. We re-analyze these CT sources using the same model presented in Sect. 2.2 and leave the inclination angle free to vary when fitting the spectra. Thus, we were able to compare the properties of the obscuring torus of CT sources with those of the Compton-thin sources in our sample. The best-fit re-analysis results of the CT sources in the M19 sample are reported in Table A.5. Four CT sources in the M19 sample are found to be Compton thin in our re-analysis. Therefore, we add those four sources to our Compton-thin sample, which now includes 89 sources in total[4].

Although CT-AGNs are an ideal sample with which to study the obscuring torus – because of their significantly suppressed line-of-sight emission, which allows clear visualization of the reprocessed emission from the torus–, we need to keep in mind the strong bias against the detection of CT-AGNs, which means that the observed CT sample is likely incomplete. Indeed, the detected fraction of CT-AGNs ($f_{\rm CT}$) in the BAT sample decreases significantly as the distance (redshift) increases ($f_{\rm CT} \approx 31\%$ at 10 Mpc and $f_{\rm CT} \approx 4\%$ at 100 Mpc; Ricci et al. 2015), suggesting that the detection of CT-AGNs is significantly biased, especially for low-luminosity CT-AGNs at large distance. Therefore, the torus properties derived from the CT sample in this work may not represent the torus properties of the whole CT-AGN population.

The main results of the spectral analysis are as follows:

- The Compton-thin sources in our sample are evenly observed in every direction considering the uncertainties as shown in Fig. 1 (upper left), suggesting that our BAT-selected Compton-thin AGN sample is an unbiased sample. In contrast, most of the CT sources in the M19 sample are observed edge-on, which is in agreement with the material distribution formalism used in the clumpy torus model which assumes that the obscuring clumps are populated in the edge-on direction (e.g., Nenkova et al. 2008; Buchner et al. 2019; Tanimoto et al. 2019).
- The torus column densities of the majority of Compton-thin sources and CT-AGNs are in the $>10^{24}$ cm^{-2} range as presented in Fig. 1 (upper right), suggesting that CT reflectors are commonly found in both Compton-thin AGNs and CT-AGNs. A similar result was also reported by Buchner et al. (2019), for example.
- The average torus column density is similar for both Compton-thin AGNs and CT-AGNs, namely $\log(N_{\rm H,tor,ave}) \sim 24.15$ (see left panel of Fig. 2), independent of the observing angle.
- We notice that the average column densities of the tori of Compton-thin sources are generally larger than their

[4] The median photon indices of the 89 sources is $\langle\Gamma\rangle = 1.67$.

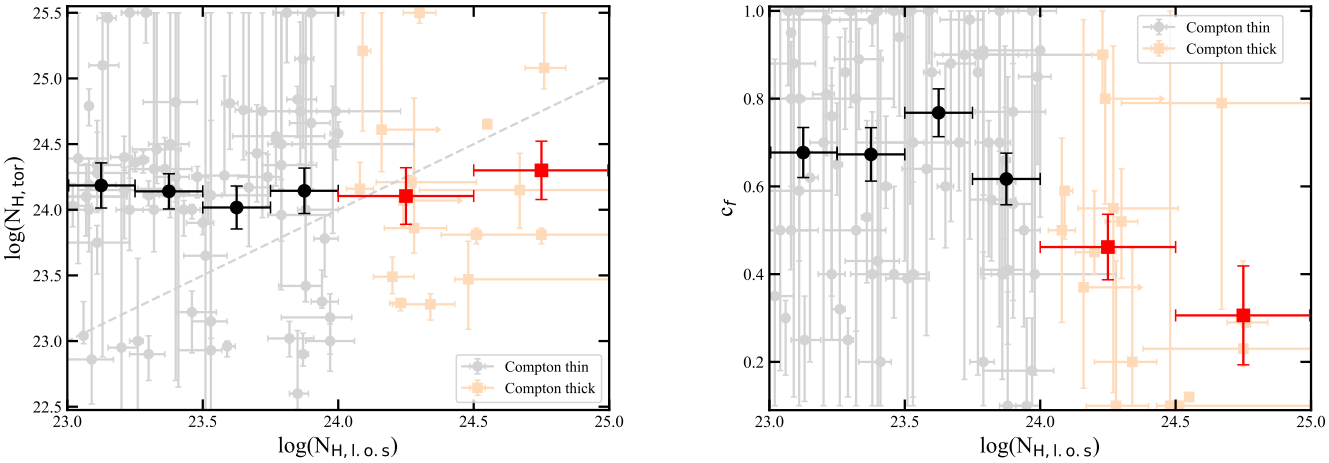

Fig. 2. Torus column density $\log(N_{\rm H,tor})$ (*left*) and torus covering factor $c_{\rm f}$ (*right*) as a function of line-of-sight column density, $\log(N_{\rm H,los})$. Compton-thin sources are plotted in light gray points, while CT sources are plotted in light red squares. The average and 1σ standard error of the torus column densities and torus covering factors in different line-of-sight column density bins are plotted in black points for Compton-thin sources and red squares for CT sources, respectively. *Left panel*: $N_{\rm H,tor} = N_{\rm H,los}$ is plotted as a light-gray dashed line. The low covering factors of the CT sources are due to the bias explained in Sect. 3.

line-of-sight column densities, suggesting that Compton-thin AGNs are usually observed through an under-dense region in their tori. Conversely, the average column densities of the tori of CT-AGNs are always smaller than their line-of-sight column densities, suggesting that CT-AGNs are observed through an over-dense region in their tori; although we cannot exclude the possibility that the additional obscuration along the line of sight of sources (especially when observed face-on) with $N_{\rm H,tor} < N_{\rm H,los}$ is due to polar outflows (Hönig et al. 2013).

– Compton-thin AGNs and CT-AGNs have (statistically) different covering factors, with the former having larger ($c_{\rm f} > 0.5$) covering factors than the latter ($c_{\rm f} < 0.5$), as shown in Fig. 1 (bottom left). Interestingly, the average torus covering factor of Compton-thin AGNs is $c_{\rm f,ave} \sim 0.67$. In contrast, the average torus covering factor decreases significantly when the line-of-sight column density reaches the CT regime, as shown in Fig. 2 (right). The low-$c_{\rm f}$ found in the CT sample might reflect the fact that the CT sample is significantly biased. The detected CT-AGNs in the BAT sample are the intrinsically most luminous sources, which typically have a lower $c_{\rm f}$ compared with the intrinsically fainter AGNs (Burlon et al. 2011; Ricci et al. 2017b; Marchesi et al. 2019), suggesting that BAT samples only the low-$c_{\rm f}$ CT-AGNs even in the nearby Universe. Indeed, Ricci et al. (2015) measured a $c_{\rm f} \approx 0.70$ for AGNs in the local Universe using a statistical method (the fraction of the absorbed AGNs is used as a proxy for the mean torus covering factor of the AGNs in the sample). Their result is in good agreement with the average covering factor measured in our unbiased Compton-thin sample.

– The obscuring material in the torus of AGNs is significantly inhomogeneous. The torus average column densities of the majority of Compton-thin AGNs and CT-AGNs are at least three times smaller or larger than their line-of-sight column densities, as shown in Fig. 1 (bottom right). Moreover, for ∼30% of sources in the sample, their torus average column densities are different from their line-of-sight column densities by more than a factor of ten. A similarly inhomogeneous torus result was found by Laha et al. (2020), who studied a sample of 20 Compton-thin AGNs.

– The distributions of the torus column density contrast ratio ($\mathrm{CR} = N_{\rm H,tor}/N_{\rm H,los}$ which shows how inhomogeneous the torus is) observed in Compton-thin AGNs and CT-AGNs are different (see, Fig. 1 bottom right). We consider that the overall distribution of the torus column density contrast ratio of different AGN types should be a combination of the CR distribution of both Compton-thin AGNs and CT-AGNs. To combine the two distributions, we rescale the torus column density contrast ratio distribution of CT-AGNs before producing the overall distribution because we are biased against the detection of CT-AGNs, that is, we need to consider the intrinsic number of Compton-thin AGNs and CT-AGNs. Here, we assume that the numbers of Compton-thin AGNs and CT-AGNs are similar, which is in agreement with the results of previous works and those found here, as discussed further in Sect. 4. After rescaling, we find that the torus column density contrast ratio is rather flat over $\mathrm{CR} = [0.03,30]$ (Fig. 1 bottom right), suggesting that for a given torus column density, an AGN can be observed with different line-of-sight column densities with equal probabilities.

In the Compton-thin sample, the effect of the biases discussed above are much weaker than in the CT sample, because the reprocessed component does not dominate the hard band emission of Compton-thin AGNs. Therefore, there is less bias in the sampling method against the tori properties measured in the Compton-thin sample. We use only these measurements to derive the intrinsic $N_{\rm H,los}$ distribution of AGNs in the local Universe in Sect. 4.

4. Intrinsic line-of-sight column density distribution of AGNs

The line-of-sight column density distribution of AGNs in the local Universe has been measured in recent years (e.g., Burlon et al. 2011; Ricci et al. 2015). However, the observed line-of-sight column density distribution is significantly affected by selection bias. Therefore, the intrinsic distribution of the AGN line-of-sight column density depends heavily on the absorption correction used, particularly for $N_{\rm H,los} > 10^{23.5}\,\mathrm{cm}^{-2}$. To investigate the actual intrinsic line-of-sight column density distribution of AGNs in the local Universe, we developed a Monte Carlo

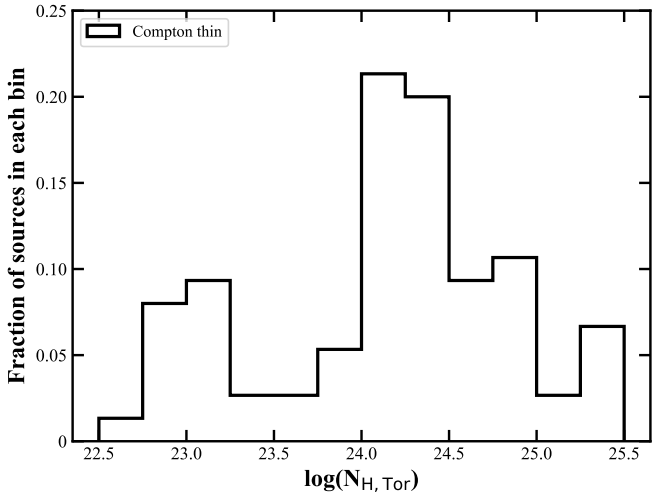

Fig. 3. Distribution of the average column density of the tori of the sources in our unbiased Compton-thin AGN sample. The histogram describes the same sample as in the upper right panel of Fig. 1 but with different grouping bins.

Table 1. Distribution of the intrinsic line-of-sight column densities derived from our new method compared with previous results from observational works and from population synthesis models.

	10^{20}–10^{22}	10^{22}–10^{26}	10^{22}–10^{24}	10^{24}–10^{26}
Our work	33%	67%	30%	37%
Observations				
	10^{20}–10^{22}	10^{22}–10^{25}	10^{22}–10^{24}	10^{24}–10^{25}
Burlon+11	38%	62%	43%	19%
Ricci+15	22%	78%	46%	32%
Population synthesis model				
	10^{20}–10^{22}	10^{22}–10^{26}	10^{22}–10^{24}	10^{24}–10^{26}
Gilli+07	13%	87%	42%	45%
Ueda+14	33%	67%	34%	33%
Buchner+15	25%	75%	37%	38%
Ananna+19	9%	91%	41%	50%

method based on the measured properties of the obscuring tori in our unbiased sample from Sect. 3. Here we assume that different types of AGNs possess tori with similar properties (Antonucci 1993; Urry & Padovani 1995). The details of our method are as follows:

1. We randomly draw a torus average column density $N_{\rm H,tor}$ from the distribution shown in Fig. 3.
2. We then assign a random contrast ratio in the range of [0.03–30] to each $N_{\rm H,tor}$ (only a small fraction of sources have extremely inhomogeneous torus with a contrast ratio outside of this range), and therefore the line-of-sight column density of each torus is $N_{\rm H,los} = N_{\rm H,tor}/{\rm CR}$;
3. We assume a 33% fraction of unobscured AGNs because the average covering factor of the torus in our sample is $c_{\rm f,ave} \sim 0.67$, and therefore the lines of sight of 33% of the AGNs do not intersect their torus. We presume that the distribution of $N_{\rm H,los}$ between 10^{20} cm^{-2} and 10^{22} cm^{-2} is flat.

A discrepancy in the intrinsic line-of-sight column density distribution between the previous observational results obtained using *Swift*-BAT (e.g., Burlon et al. 2011; Ricci et al. 2015) and constraints from different population synthesis models (e.g., Gilli et al. 2007; Ueda et al. 2014; Buchner et al. 2015; Ananna et al. 2019) still exists. We compare our derived intrinsic line-of-sight column density distribution with the results of these authors[5] in Table 1 and Fig. 4.

When comparing to the *Swift*-BAT observed column density distributions (Burlon et al. 2011; Ricci et al. 2015), our method predicts a larger fraction of CT-AGNs (see, Table 1), which is likely because of the difficulty that *Swift*-BAT has in detecting extremely heavily obscured AGNs. Our predictions are in good agreement with the column density distribution used in the population synthesis model in Ueda et al. (2014), which is also based on a low-redshift *Swift*-BAT-selected sample. It is worth noting that the column density distribution is luminosity (and redshift) dependent (see, e.g., Buchner et al. 2015). Different works adopt different samples of AGNs with different luminosity and redshift ranges when deriving the column density distribution. In particular, our work provides a constraint on the line-of-sight column density distribution of AGNs with a median 2–10 keV intrinsic luminosity of $\langle L_{\rm int,2-10}\rangle = 1.20 \times 10^{43}$ erg s^{-1} in the local Universe ($z < 0.15$). The listed column density distributions of each of the studies in Table 1 are the values at $z \sim 0$. We note that the fraction of unobscured AGNs derived in our work at $z \sim 0$ is larger than those obtained in Gilli et al. (2007), Buchner et al. (2015), Ananna et al. (2019). Therefore, an overestimation of the CXB at the soft X-ray band might occur if the fraction of unobscured AGNs is consistent at different redshifts, suggesting that the unobscured AGN fraction should significantly decrease, moving towards higher redshifts, as discovered in observations (e.g., Lanzuisi et al. 2018).

Figure 5 shows a comparison of the average torus properties obtained from our unbiased sample (left side) and the intrinsic line-of-sight column density distribution derived from our method.

5. Conclusions

We study the obscuring tori of AGNs by analyzing the broadband X-ray spectra of a large and unbiased sample of heavily obscured AGNs in the local Universe. We find that Compton-thin AGNs and CT-AGNs may possess similar tori, whose average column density is Compton thick ($N_{\rm H,tor,ave} \approx 1.4 \times 10^{24}$ cm^{-2}), but that they are observed through different (under-dense or over-dense) regions of the tori. The average torus covering factor of the Compton-thin sample is $c_{\rm f} = 0.67$, suggesting that the fraction of unobscured AGNs is ~33%. We also find that the obscuring tori of most AGNs are significantly inhomogeneous. Using the obtained properties of the obscuring torus and a Monte Carlo method, we calculate the intrinsic line-of-sight column density distribution of AGNs in the nearby Universe, finding good agreement with recent AGN population synthesis models. Our results may help understand the properties of the obscuring materials surrounding the SMBH in the local Universe and help to constrain the future population synthesis study of the CXB. In the future, new X-ray missions such as *Athena* and the proposed Lynx and AXIS facilities will detect a large sample of obscured AGNs at high redshift (see, e.g., Marchesi et al. 2020), which could help us to further constrain the evolution of AGN obscuration and SMBH growth over cosmic time.

[5] The reported observational column density distributions are those that have been corrected for selection bias and for the bias against detecting extremely absorbed sources. The average redshifts of the sources in the samples used in Burlon et al. (2011) and Ricci et al. (2015) are $\langle z\rangle = 0.03$ and 0.055, respectively.

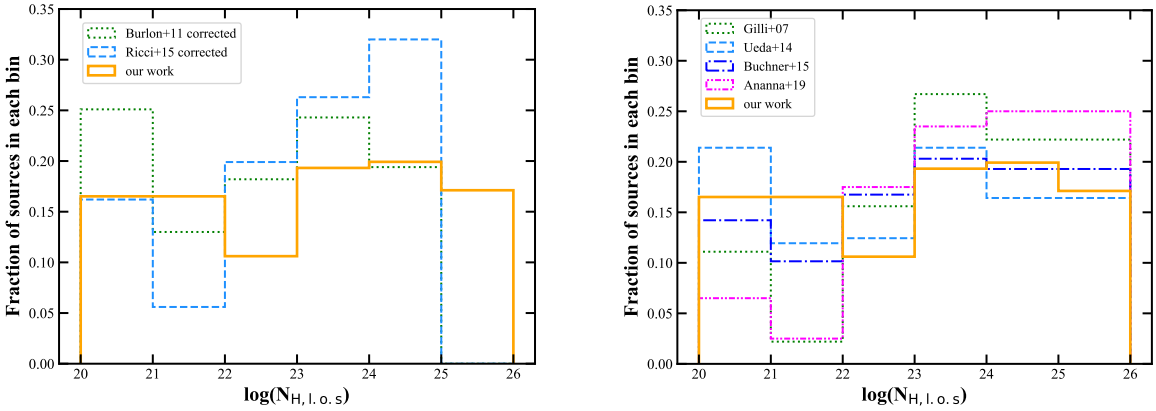

Fig. 4. Comparison between the distributions of intrinsic line-of-sight column density derived from our new developed method with previous observational results (*left*) and those used in different population synthesis models (*right*). The extremely obscured sources with $\log(N_{\rm H,los}) > 26$ are included in the $25 < \log(N_{\rm H,los}) < 26$ bin.

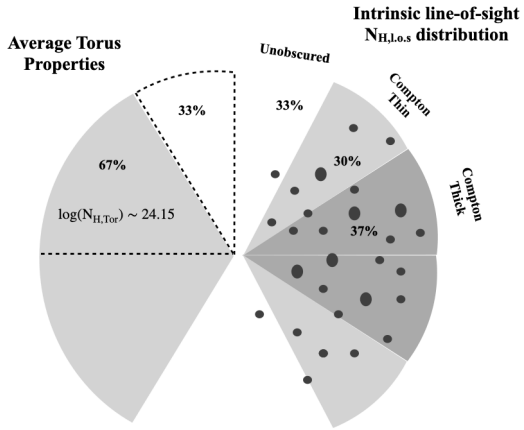

Fig. 5. Average torus properties of our unbiased Compton-thin sample (*left*) and intrinsic line-of-sight column density distribution derived from our new developed method (*right*).

Acknowledgements. X.Z. thanks the anonymous referee for their detailed and useful comments, which helped improve the paper significantly. X.Z., M.A. and S.M. acknowledge NASA funding under contract 80NSSC17K0635 and 80NSSC19K0531. X.Z. also acknowledges NASA funding under contract 80NSSC20K0043. This research has made use of the Palermo BAT Catalogue and database operated at INAF-IASF Palermo. We thank the *NuSTAR* Operations, Software and Calibrations teams for support with these observations. This research has made use of data and/or software provided by the High Energy Astrophysics Science Archive Research Center (HEASARC), which is a service of the Astrophysics Science Division at NASA/GSFC and the High Energy Astrophysics Division of the Smithsonian Astrophysical Observatory. This work is based on observations obtained with *XMM-Newton*, an ESA science mission with instruments and contributions directly funded by ESA Member States and NASA. The scientific results reported in this article are based in part on observations made by data obtained from the *Chandra* Data Archive. This work made use of data supplied by the UK *Swift* Science Data Centre at the University of Leicester.

References

Almeida, C. R., & Ricci, C. 2017, Nat. Astron., 1, 679
Ananna, T. T., Treister, E., Urry, C. M., et al. 2019, ApJ, 871, 240
Anders, E., & Grevesse, N. 1989, Geochim. Cosmochim. Acta, 53, 197
Antonucci, R. 1993, ARA&A, 31, 473
Arnaud, K. A. 1996, Astronomical Data Analysis Software and Systems V, 101, 17
Baloković, M., Brightman, M., Harrison, F. A., et al. 2018, ApJ, 854, 42
Bianchi, S., Maiolino, R., & Risaliti, G. 2012, Adv. Astron., 2012, 17
Buchner, J., Georgakakis, A., Nandra, K., et al. 2015, ApJ, 802, 89
Buchner, J., Brightman, M., Nandra, K., Nikutta, R., & Bauer, F. 2019, A&A, 629, A16
Burlon, D., Ajello, M., Greiner, J., et al. 2011, ApJ, 728, 58
Cash, W. 1979, ApJ, 228, 939
Circosta, C., Vignali, C., Gilli, R., et al. 2019, A&A, 623, A172
Civano, F., Hickox, R. C., Puccetti, S., et al. 2015, ApJ, 808, 185
Comastri, A., Setti, G., Zamorani, G., & Hasinger, G. 1995, A&A, 296, 1
Di Matteo, T., Springel, V., & Hernquist, L. 2005, Nature, 433, 604
Evans, P. A., Beardmore, A. P., Page, K. L., et al. 2009, MNRAS, 397, 1177
Fruscione, A., McDowell, J. C., Allen, G. E., et al. 2006, Proc. SPIE, 6270, 62701V
Gilli, R., Comastri, A., & Hasinger, G. 2007, A&A, 463, 79
Guainazzi, M. 2002, MNRAS, 329, L13
Hickox, R. C., & Alexander, D. M. 2018, ARA&A, 56, 625
Hönig, S. F., Kishimoto, M., Tristram, K. R. W., et al. 2013, ApJ, 771, 87
Jansen, F., Lumb, D., Altieri, B., et al. 2001, A&A, 365, L1
Kalberla, P. M. W., Burton, W. B., Hartmann, D., et al. 2005, A&A, 440, 775
Laha, S., Markowitz, A. G., Krumpe, M., et al. 2020, ApJ, 897, 66
Lansbury, G. B., Alexander, D. M., Aird, J., et al. 2017, ApJ, 846, 20
Lanzuisi, G., Civano, F., Marchesi, S., et al. 2018, MNRAS, 480, 2578
Maccacaro, T., della Ceca, R., Gioia, I. M., , et al. 1991, ApJ, 374, 117
Madau, P., Ghisellini, G., & Fabian, A. C. 1994, MNRAS, 270, L17
Marchesi, S., Lanzuisi, G., Civano, F., et al. 2016, ApJ, 830, 100
Marchesi, S., Ajello, M., Marcotulli, L., et al. 2018, ApJ, 854, 49
Marchesi, S., Ajello, M., Zhao, X., et al. 2019, ApJ, 872, 8
Marchesi, S., Gilli, R., Lanzuisi, G., et al. 2020, A&A, 642, A184
Markowitz, A. G., Krumpe, M., & Nikutta, R. 2014, MNRAS, 439, 1403
Masini, A., Civano, F., Comastri, A., et al. 2018, ApJS, 235, 17
Mason, R. E., Levenson, N. A., Shi, Y., et al. 2009, ApJ, 693, L136
Mewe, R., Gronenschild, E. H. B. M., & van den Oord, G. H. J. 1985, A&AS, 62, 197
Nandra, K. 2001, Adv. Space Res., 28, 295
Nenkova, M., Ivezić, Ž., & Elitzur, M. 2002, ApJ, 570, L9
Nenkova, M., Sirocky, M. M., Ivezić, Ž., & Elitzur, M. 2008, ApJ, 685, 147
Netzer, H. 2015, ARA&A, 53, 365
Noguchi, K., Terashima, Y., Ishino, Y., et al. 2010, ApJ, 711, 144
Ricci, C., Ueda, Y., Koss, M. J., et al. 2015, ApJ, 815, L13
Ricci, C., Trakhtenbrot, B., Koss, M. J., et al. 2017a, ApJS, 233, 17
Ricci, C., Trakhtenbrot, B., Koss, M. J., et al. 2017b, Nature, 549, 488
Richstone, D., Ajhar, E. A., Bender, R., et al. 1998, Nature, 385, A14
Risaliti, G. 2002, A&A, 386, 379
Risaliti, G., Maiolino, R., & Salvati, M. 1999, ApJ, 522, 157
Risaliti, G., Elvis, M., & Nicastro, F. 2002, ApJ, 571, 234
Soltan, A. 1982, MNRAS, 200, 115
Strüder, L., Briel, U., Dennerl, K., et al. 2001, A&A, 365, L18
Tanimoto, A., Ueda, Y., Odaka, H., et al. 2019, ApJ, 877, 95
Tristram, K. R. W., Meisenheimer, K., Jaffe, W., et al. 2007, A&A, 474, 837
Turner, M. J. L., Abbey, A., Arnaud, M., et al. 2001, A&A, 365, L27
Ueda, Y., Akiyama, M., Hasinger, G., Miyaji, T., & Watson, M. G. 2014, ApJ, 786, 104
Urry, C. M., & Padovani, P. 1995, PASP, 107, 803
Verner, D., Ferland, G., Korista, K., & Yakovlev, D. 1996, ApJ, 465, 487
Wada, K., Schartmann, M., & Meijerink, R. 2016, ApJ, 828, L19
Zappacosta, L., Comastri, A., Civano, F., et al. 2018, ApJ, 854, 33
Zhao, X., Marchesi, S., & Ajello, M. 2019a, ApJ, 871, 182
Zhao, X., Marchesi, S., Ajello, M., et al. 2019b, ApJ, 870, 60
Zhao, X., Marchesi, S., Ajello, M., Baloković, M., & Fischer, T. 2020, ApJ, 894, 71

Appendix A: Data reduction and spectral analysis results

Information about the observations adopted when analyzing each source is listed in Tables A.1. The redshift of each source is adopted from NED[6] and SIMBAD[7], except for 2MASX J00502684+8229000, for which there is no redshift record; we therefore let the redshift of this source free to vary when fitting its spectra obtain a best-fit redshift of $z \sim 0.03817$.

The *NuSTAR* data of both FPMA and FPMB are calibrated, cleaned, and screened using the `nupipeline` script version 0.4.6 and calibration database (CALDB) version 20181030. The sources spectra, ancillary response files (ARF), and response matrix files (RMF) are obtained using the `nuproducts` script version 0.3.0. The source spectra are extracted from a 75″ circular region, and the background spectra are extracted using a 75″ circular region near the source but avoiding contamination from the source.

The *XMM-Newton* data from two MOS cameras (Turner et al. 2001) and one EPIC CCD camera (pn; Strüder et al. 2001) onboard *XMM-Newton* are utilized in the spectral analysis. The *XMM-Newton* data are reduced using the Science Analysis System (SAS; Jansen et al. 2001) version 17.0.0 following standard procedures. The flares are removed by visually inspecting the high-energy light curve (10–12 keV) when the count rates exceed 0.35 cts s^{-1} for MOS and 0.4 cts s^{-1} for pn. The source spectra are extracted from a circular region with a radius of 15″; the background spectra are extracted from a circle nearby the source with the same radius as the source spectra but avoiding contamination from sources.

Chandra data, focused on the 0.3–7 keV energy band, are used in our spectral analysis when *XMM-Newton* data are not available. We reduced the *Chandra* data using the *Chandra*'s data analysis system, CIAO software package (Fruscione et al. 2006) version 4.11 and *Chandra* CALDB version 4.8.2. The level=1 data are reprocessed using the CIAO `chandra_repro` script. The source spectrum is extracted from a circular region with a radius of 5″; the background spectrum is extracted from a circular region near the source with a radius of 10″. The CIAO `specextract` tool is used to extract both source and background spectra, ARF, and RMF files following standard procedures.

Given the smaller effective area in soft X-ray band (eight times smaller than *XMM-Newton* pn and four times smaller than *Chandra* at 3 keV), *Swift*-XRT data are used only when neither *XMM-Newton* nor *Chandra* data are available. The spectra are obtained from the online *Swift* product generator[8] (see also Evans et al. 2009). In the case of variability, we did not stack multiple observations of the same source. The *Swift*-XRT spectra are rebinned with a minimum of 5 counts per bin because of the limited number of counts using the HEAsoft task `grppha`, while the *NuSTAR*, *XMM-Newton*, and *Chandra* spectra are rebinned with a minimum of 20 counts per bin.

Table A.1. 93 BAT selected sources with archival *NuSTAR* observations.

Source	z	*NuSTAR* date	*NuSTAR* ks	XMM date	XMM ks	*Chandra* date	*Chandra* ks	XRT date	XRT ks
2MASX J00502684+8229000	N/A [(a)]	2018 Aug 25	54					2018 Aug 25	7
2MASX J01073963−1139117	0.04746	2016 Sep 16	42			2019 May 21	10		
2MASX J06411806+3249313	0.04700	2018 Dec 31	36	2006 Mar 11	17				
2MASX J09235371−3141305	0.04237	2014 Apr 20	42					2014 Apr 19	7
2MASX J11140245+2023140	0.02615	2014 Jan 17	48					2014 Jan 17	6
3C 105	0.08900	2016 Aug 21	42	2008 Feb 25	34				
3C 403	0.05900	2013 May 25	40			2002 Dec 07	49		
3C 445	0.05588	2016 May 15	40	2001 Dec 06	57				
3C 452	0.08110	2017 May 01	104	2008 Nov 30	194				
4C +29.30	0.06471	2013 Nov 08	42	2008 Apr 11	62				
4C +73.08	0.05810	2016 Dec 05	26			2009 July 11	29		
CASG218	0.05395	2016 Dec 31	40			2016 Dec 26	23		
Cen A	0.00183	2013 Aug 06	102	2013 Aug 07	29				
CGCG 427-028	0.03033	2014 Dec 10	52	2014 Dec 10	84				
ESO 21-4	0.00984	2015 May 05	42					2019 Dec 22	6
ESO 103-35	0.01329	2017 Oct 15	88	2002 Mar 15	30				
ESO 119-8	0.02294	2016 Jun 27	52			2016 July 09	10		
ESO 121-28	0.04052	2014 Aug 08	44					2014 Aug 08	7
ESO 231-26	0.06254	2015 Mar 13	48					2009 Jun 19	2
ESO 263-13	0.03354	2015 Oct 13	46	2007 Jun 14	61				
ESO 317-41	0.01932	2018 May 27	62	2018 May 27	72				
ESO 383-18	0.01241	2016 Jan 20	213	2006 Jan 10	45				
ESO 439-G009	0.02389	2015 Dec 20	46	2015 Jun 07	34				
ESO 464-16	0.03635	2016 Apr 13	44	2016 Apr 11	55				
ESO 500-34	0.01222	2017 Dec 15	36			2016 Feb 08	10		
ESO 505-30	0.03971	2018 Jan 28	44					2018 Jan 28	7
ESO 553-43	0.02776	2016 Aug 16	43					2010 May 16	10
Fairall 272	0.02182	2014 Jan 10	48	2007 Oct 14	30				
IC 751	0.03120	2014 Nov 28	52	2014 Nov 28	64				
IC 1657	0.01195	2017 Jan 15	90					2008 Nov 03	2

Notes. Column 2: redshift of the source. Columns 3–4: *NuSTAR* observation date and exposure time. Columns 5–6: *XMM-Newton* observation date and exposure time. Columns 7–8: *Chandra* observation date and exposure time. Columns 9–10: XRT observation date and exposure time. [(a)]No redshift record is found for 2MASX J00502684+8229000 in either NED or SIMBAD, so we let the redshift free to vary when fitting the spectra. The best-fit redshift is $z \sim 0.03817$.

[6] https://ned.ipac.caltech.edu
[7] http://simbad.u-strasbg.fr/simbad/
[8] https://www.swift.ac.uk/user_objects/

Table A.1. continued.

Source	z	*NuSTAR* date	*NuSTAR* ks	XMM date	XMM ks	*Chandra* date	*Chandra* ks	XRT date	XRT ks
IC 4709	0.01690	2013 July 24	40					2006 Oct 28	2
IC 4518A	0.01626	2013 Aug 02	16	2006 Aug 07	22				
IC 5063	0.01135	2013 July 08	36			2007 Jun 15	34		
IRAS 05581+0006	0.11470	2015 Dec 12	42					2010 May 07	10
IRAS 16288+3929	0.03056	2012 Sep 19	32	2011 Sep 08	78				
IRAS 20247−7542	0.11394	2019 Feb 18	70					2010 July 02	7
LEDA 15023	0.04500	2012 July 24	12			2012 Oct 20	19		
LEDA 2265450	0.02678	2014 Dec 23	40					2006 Jan 04	6
LEDA 259433	0.09001	2019 Mar 01	44					2009 Dec 31	7
LEDA 2816387	0.10756	2016 May 06	53	2017 Nov 20	50				
LEDA 46599	0.03194	2016 Jan 09	42					2016 Jan 09	6
LEDA 511869	0.07661	2016 May 25	44	2018 Feb 09	41				
LEDA 549777	0.06100	2014 Jan 21	44					2006 Jun 23	12
MCG -01-05-047	0.01720	2012 Nov 30	26	2009 July 24	30				
MCG -02-09-040	0.01499	2015 Feb 25	44	2015 Feb 25	26				
MCG -02-15-004	0.02897	2018 Nov 13	40					2010 May 05	6
MCG -03-34-064	0.01654	2016 Jan 17	157	2016 Jan 17	372				
MCG +11-11-32	0.03625	2016 Feb 18	8					2015 Dec 14	7
Mrk 3	0.01351	2015 Apr 08	50	2015 Apr 08	8				
Mrk 18	0.01109	2013 Dec 15	40	2006 Mar 23	36				
Mrk 273	0.03778	2013 Nov 04	140	2013 Nov 04	19				
Mrk 348	0.01503	2015 Oct 28	42	2002 July 18	76				
Mrk 417	0.03276	2017 Feb 20	42	2006 Jun 15	24				
Mrk 477	0.03773	2014 May 15	36	2010 July 21	30				
...	...	2014 May 24	34	...	...				
Mrk 1210	0.01350	2012 Oct 05	30	2001 May 05	18				
Mrk 1498	0.05470	2015 May 11	48	2007 Jun 23	21				
NGC 454E	0.01213	2016 Feb 14	48	2009 Nov 05	76				
NGC 612	0.02977	2012 Sep 14	30	2006 Jun 26	71				
NGC 788	0.01360	2013 Jan 28	30	2010 Jan 15	71				
NGC 835	0.01359	2015 Sep 13	42	2000 Jan 23	91				
NGC 1142	0.02885	2017 Oct 14	41	2006 Jan 28	32				
NGC 1229	0.03629	2013 July 05	50					2010 Oct 19	7
NGC 2655	0.00467	2016 Nov 10	32	2005 Sep 04	16				
NGC 3281	0.01067	2016 Jan 22	46	2011 Jan 05	64				
NGC 4102	0.00282	2015 Nov 19	42			2016 Jun 17	29		
NGC 4258	0.00149	2016 Jan 10	208	2006 Nov 17	142				
NGC 4388	0.00842	2013 Dec 27	42			2008 Apr 16	171		
NGC 4500	0.01038	2015 Aug 30	42					2015 Aug 30	7
NGC 4507	0.01180	2015 Jun 10	68	2010 Aug 03	29				
NGC 4785	0.01227	2014 Aug 20	98	2014 Aug 20	72				
NGC 4939	0.01037	2017 Feb 17	44			2010 Jun 09	14		
NGC 4941	0.00370	2016 Jan 19	42			2011 Mar 07	5		
NGC 4992	0.02514	2015 Jan 27	46	2006 Jun 27	45				
NGC 5283	0.01040	2018 Nov 17	66			2003 Nov 24	9		
NGC 5728	0.00935	2013 Jan 02	48			2003 Jun 27	19		
NGC 5899	0.00855	2014 Apr 08	48	2011 Feb 13	62				
NGC 5972	0.02974	2018 Mar 20	83			2017 Dec 18	24		
...	...	...	...			2017 Dec 19	24		
NGC 6300	0.00370	2016 Aug 24	48	2001 Mar 02	128				
NGC 6232	0.01480	2013 Aug 17	38					2011 Apr 29	3
NGC 7319	0.02251	2017 Sep 27	84	2001 Dec 07	121				
PKS 2356-61	0.09631	2014 Aug 10	46	2011 Oct 19	22	2010 Mar 04	20		
SDSS J135429.05+132757.2	0.06332	2019 Mar 14	39			2014 Jun 25	9		
SDSS J165315.05+234942.9	0.10342	2018 Jan 19	56	2011 Mar 09	35				
UGC 3157	0.01541	2014 Mar 18	40					2010 Oct 22	6
UGC 3752	0.01569	2013 Dec 03	48					2013 Dec 03	7
UGC 3995B	0.01597	2014 Nov 08	46			2014 Feb 07	11		
UGC 4211	0.03443	2017 Mar 11	40			2019 Feb 08	10		
VII Zw 73	0.04133	2012 Nov 08	34	2011 Mar 04	27				
Was 49b	0.06400	2014 July 15	40			2014 July 15	6		
WISE J144850.99-400845.6	0.12323	2019 Mar 12	40	2014 Feb 16	67				
Z319-7	0.04400	2014 May 01	30					2014 May 01	7
Z333-49	0.03358	2015 Jan 15	50					2009 Jan 14	10
Z367-9	0.02392	2014 Dec 21	60					2007 May 30	10

Table A.2. Best-fit results of the sources with *NuSTAR* (3–78 keV) data and *XMM-Newton* (1–10 keV) data.

Source	χ^2/d.o.f.	Γ	$N_{\rm H,los}$	$N_{\rm H,tor}$	$\cos(\theta_{\rm inc})$	$c_{\rm f}$	Norm	$\rm Flux_{2-10}$	$L_{\rm int,2-10}$
2MASX J06411806+3249313	382/371	$1.60^{+0.09}_{-0.08}$	$23.09^{+0.08}_{-0.10}$	$22.86^{+0.89}_{-0.34}$	0.95^{+u}_{-u}	$0.88^{+u}_{-0.76}$	$0.16^{+0.04}_{-0.03}$	$-11.27^{+0.04}_{-0.08}$	$43.70^{+0.05}_{-0.05}$
3C 105*	205/232	$1.53^{+0.13}_{-0.13}$	$23.65^{+0.03}_{-0.03}$	–	–	–	$0.25^{+0.10}_{-0.07}$	$-12.03^{+0.02}_{-0.05}$	$43.97^{+0.07}_{-0.07}$
3C 445	885/913	$1.56^{+0.05}_{-0.14}$	$23.08^{+0.05}_{-0.07}$	$24.00^{+0.11}_{-0.32}$	$0.95^{+u}_{-0.08}$	$0.80^{+0.12}_{-0.20}$	$0.22^{+0.02}_{-0.04}$	$-11.27^{+0.02}_{-0.08}$	$43.76^{+0.01}_{-0.01}$
3C 452	1206/1177	$1.49^{+0.02}_{-0.02}$	$23.59^{+0.03}_{-0.01}$	$22.96^{+0.04}_{-0.08}$	$0.95^{+u}_{-0.09}$	$1.00^{+u}_{-0.12}$	$0.26^{+0.02}_{-0.01}$	$-11.51^{+0.01}_{-0.02}$	$44.36^{+0.02}_{-0.01}$
4C +29.30	168/176	$1.46^{+0.21}_{-u}$	$23.50^{+0.04}_{-0.06}$	$23.90^{+0.11}_{-0.09}$	0.55^{+u}_{-u}	$1.00^{+u}_{-0.57}$	$0.05^{+0.04}_{-0.01}$	$-12.00^{+0.01}_{-0.51}$	$43.35^{+0.13}_{-0.05}$
Cen A	5100/4781	$1.81^{+0.01}_{-0.01}$	$23.06^{+0.01}_{-0.01}$	$23.04^{+0.26}_{-0.06}$	$0.35^{+0.15}_{-0.04}$	$0.30^{+0.04}_{-0.13}$	$9.95^{+0.07}_{-0.14}$	$-9.36^{+0.01}_{-0.01}$	$42.82^{+0.01}_{-0.01}$
CGCG 427-028	463/470	$1.76^{+0.03}_{-0.09}$	$23.15^{+0.03}_{-0.04}$	$25.46^{+u}_{-1.12}$	$0.60^{+0.31}_{-0.40}$	$0.62^{+0.06}_{-0.42}$	$0.11^{+0.01}_{-0.02}$	$-11.66^{+0.02}_{-0.03}$	$42.99^{+0.03}_{-0.03}$
ESO 103-35	2006/1907	$1.70^{+0.10}_{-0.08}$	$23.25^{+0.02}_{-0.02}$	$24.36^{+0.08}_{-0.07}$	$0.51^{+0.16}_{-0.05}$	$0.65^{+0.14}_{-0.07}$	$1.73^{+0.34}_{-0.16}$	$-10.74^{+0.01}_{-0.06}$	$43.37^{+0.02}_{-0.02}$
ESO 263-13	410/444	$1.64^{+0.12}_{-0.12}$	$23.85^{+0.04}_{-0.03}$	$22.60^{+0.48}_{-0.12}$	$0.64^{+0.20}_{-u}$	$0.70^{+u}_{-0.42}$	$0.24^{+0.01}_{-0.01}$	$-11.87^{+0.01}_{-0.07}$	$43.50^{+0.04}_{-0.05}$
ESO 317-41	158/156	$1.76^{+0.31}_{-0.21}$	$23.90^{+0.07}_{-0.08}$	$24.66^{+u}_{-0.50}$	$0.45^{+0.36}_{-u}$	$0.56^{+u}_{-0.26}$	$0.12^{+0.16}_{-0.07}$	$-12.36^{+0.17}_{-u}$	$42.60^{+0.18}_{-0.29}$
ESO 383-18	1367/1343	$1.58^{+0.04}_{-0.05}$	$23.28^{+0.03}_{-0.02}$	$24.38^{+0.07}_{-0.10}$	$0.84^{+0.07}_{-0.15}$	$0.86^{+0.10}_{-0.13}$	$0.39^{+0.04}_{-0.04}$	$-11.34^{+0.02}_{-0.04}$	$42.54^{+0.03}_{-0.02}$
ESO 439-G009	173/180	$1.77^{+0.26}_{-0.19}$	$23.58^{+0.09}_{-0.09}$	$24.26^{+u}_{-0.15}$	$0.10^{+0.67}_{-u}$	$0.64^{+u}_{-0.38}$	$0.16^{+0.16}_{-0.07}$	$-11.93^{+0.17}_{-0.35}$	$42.89^{+0.14}_{-0.16}$
ESO 464-16	137/131	$1.46^{+0.30}_{-u}$	$23.79^{+0.18}_{-0.05}$	$23.96^{+0.27}_{-0.20}$	$0.74^{+0.11}_{-u}$	$0.91^{+u}_{-0.52}$	$0.04^{+0.05}_{-0.09}$	$-12.27^{+0.08}_{-u}$	$42.97^{+0.19}_{-0.10}$
Fairall 272	559/594	$1.51^{+0.11}_{-0.08}$	$23.23^{+0.05}_{-0.05}$	$24.00^{+0.33}_{-0.31}$	$0.37^{+0.21}_{-u}$	$0.40^{+0.47}_{-0.15}$	$0.18^{+0.06}_{-0.04}$	$-11.19^{+0.06}_{-0.20}$	$43.10^{+0.06}_{-0.04}$
IC 4518A	188/186	$1.72^{+0.15}_{-0.18}$	$23.11^{+0.12}_{-0.16}$	$24.28^{+0.40}_{-0.30}$	$0.75^{+0.16}_{-u}$	$0.80^{+u}_{-0.37}$	$0.20^{+0.09}_{-0.06}$	$-11.37^{+0.03}_{-0.09}$	$42.75^{+0.06}_{-0.09}$
IC 751	280/257	$2.06^{+0.15}_{-0.14}$	$23.60^{+0.03}_{-0.03}$	$24.76^{+u}_{-0.30}$	$0.59^{+0.27}_{-u}$	$0.72^{+u}_{-0.24}$	$0.28^{+0.09}_{-0.10}$	$-11.93^{+0.10}_{-0.07}$	$43.20^{+0.06}_{-0.09}$
IRAS 16288+3929	187/196	$1.72^{+0.12}_{-0.17}$	$23.88^{+0.06}_{-0.10}$	$23.42^{+0.69}_{-0.12}$	$0.26^{+0.47}_{-u}$	$0.41^{+0.44}_{-0.17}$	$0.23^{+0.11}_{-0.11}$	$-12.06^{+0.06}_{-0.07}$	$43.28^{+0.17}_{-0.19}$
LEDA 2816387*	243/232	$1.33^{+0.13}_{-0.12}$	$23.76^{+0.05}_{-0.07}$	–	–	–	$0.08^{+0.04}_{-0.03}$	$-12.00^{+0.01}_{-0.09}$	$44.24^{+0.11}_{-0.10}$
LEDA 511869	157/155	$1.49^{+0.18}_{-u}$	$23.88^{+0.12}_{-0.03}$	$24.00^{+u}_{-0.70}$	$0.13^{+0.13}_{-0.06}$	$0.10^{+0.26}_{-u}$	$0.22^{+0.23}_{-0.05}$	$-11.24^{+0.03}_{-0.61}$	$43.92^{+0.07}_{-0.06}$
MCG -01-05-047	251/261	$1.89^{+0.10}_{-0.12}$	$23.33^{+0.09}_{-0.09}$	$24.46^{+u}_{-0.26}$	$0.89^{+0.05}_{-0.20}$	$0.89^{+0.07}_{-0.16}$	$0.30^{+0.08}_{-0.07}$	$-11.58^{+0.04}_{-0.06}$	$42.68^{+0.04}_{-0.04}$
MCG -02-09-040	111/92	$1.95^{+0.39}_{-0.15}$	$23.90^{+0.12}_{-0.14}$	$25.50^{+u}_{-1.14}$	$0.86^{+u}_{-0.52}$	$0.77^{+0.11}_{-0.43}$	$0.12^{+0.38}_{-0.07}$	$-12.31^{+0.01}_{-u}$	$42.26^{+0.24}_{-0.34}$
MCG -03-34-064	1920/1460	$1.92^{+0.02}_{-0.02}$	$23.77^{+0.02}_{-0.01}$	$24.53^{+0.03}_{-0.05}$	$0.85^{+0.01}_{-0.00}$	$0.86^{+0.04}_{-0.00}$	$0.48^{+0.01}_{-0.03}$	$-11.68^{+0.02}_{-0.06}$	$42.92^{+0.01}_{-0.01}$
Mrk 3	1056/1073	$1.48^{+0.11}_{-u}$	$23.94^{+0.06}_{-0.04}$	$23.30^{+0.24}_{-0.05}$	$0.47^{+0.16}_{-0.07}$	$0.50^{+0.06}_{-0.22}$	$1.42^{+0.54}_{-0.22}$	$-11.01^{+0.01}_{-1.05}$	$43.42^{+0.05}_{-0.04}$
Mrk 18	212/204	$1.70^{+0.15}_{-0.23}$	$23.13^{+0.06}_{-0.05}$	$25.10^{+u}_{-2.22}$	$0.95^{+u}_{-0.63}$	$0.25^{+0.10}_{-0.14}$	$0.07^{+0.02}_{-0.01}$	$-11.97^{+0.03}_{-0.23}$	$41.76^{+0.05}_{-0.05}$
Mrk 273	339/359	$1.76^{+0.20}_{-0.20}$	$23.52^{+0.05}_{-0.09}$	$24.11^{+0.10}_{-0.22}$	0.15^{+u}_{-u}	$1.00^{+u}_{-0.44}$	$0.06^{+0.00}_{-0.03}$	$-12.09^{+0.01}_{-0.27}$	$42.90^{+0.14}_{-0.12}$
Mrk 348	2702/2583	$1.66^{+0.03}_{-0.03}$	$22.92^{+0.03}_{-0.04}$	$24.48^{+0.48}_{-0.54}$	$0.21^{+0.02}_{-0.03}$	$0.17^{+0.08}_{-u}$	$1.33^{+0.09}_{-0.08}$	$-10.43^{+0.01}_{-0.01}$	$43.48^{+0.04}_{-0.08}$
Mrk 417	314/326	$1.57^{+0.08}_{-0.09}$	$23.53^{+0.06}_{-0.07}$	$23.15^{+1.53}_{-0.25}$	$0.15^{+0.26}_{-u}$	$0.40^{+0.21}_{-u}$	$0.23^{+0.04}_{-0.05}$	$-11.51^{+0.01}_{-0.05}$	$43.46^{+0.01}_{-0.01}$
Mrk 477	673/539	$1.58^{+0.09}_{-0.07}$	$23.30^{+0.06}_{-0.07}$	$22.90^{+0.14}_{-0.20}$	0.95^{+u}_{-u}	$1.00^{+u}_{-0.22}$	$0.16^{+0.06}_{-0.03}$	$-11.47^{+0.01}_{-0.01}$	$43.36^{+0.05}_{-0.05}$
Mrk 1210	679/669	$1.77^{+0.06}_{-0.03}$	$23.30^{+0.04}_{-0.02}$	$24.11^{+0.11}_{-0.08}$	0.95^{+u}_{-u}	$1.00^{+u}_{-0.07}$	$0.74^{+0.15}_{-0.11}$	$-11.12^{+0.01}_{-0.02}$	$42.92^{+0.03}_{-0.03}$
Mrk 1498	811/815	$1.67^{+0.04}_{-0.04}$	$23.26^{+0.02}_{-0.03}$	$23.00^{+0.63}_{-0.70}$	$0.95^{+u}_{-0.62}$	$0.32^{+0.62}_{-u}$	$0.42^{+0.05}_{-0.05}$	$-11.10^{+0.01}_{-0.02}$	$44.12^{+0.02}_{-0.02}$
NGC 454E	344/310	$1.81^{+0.11}_{-0.11}$	$23.86^{+0.04}_{-0.04}$	$24.75^{+0.68}_{-0.40}$	$0.43^{+0.16}_{-0.11}$	$0.40^{+0.26}_{-0.24}$	$0.16^{+0.06}_{-0.03}$	$-12.18^{+0.02}_{-0.15}$	$42.26^{+0.04}_{-0.04}$
NGC 612	176/195	$1.54^{+0.12}_{-0.08}$	$23.95^{+0.05}_{-0.04}$	$23.78^{+0.18}_{-0.29}$	$0.05^{+0.01}_{-u}$	$0.10^{+0.20}_{-u}$	$0.53^{+0.30}_{-0.02}$	$-11.96^{+0.02}_{-0.21}$	$43.56^{+0.14}_{-0.02}$
NGC 788	303/290	$1.56^{+0.14}_{-0.16}$	$23.79^{+0.04}_{-0.05}$	$24.50^{+u}_{-1.11}$	$0.26^{+0.08}_{-0.03}$	$0.20^{+0.25}_{-u}$	$0.45^{+0.18}_{-0.15}$	$-11.71^{+0.01}_{-0.25}$	$42.97^{+0.07}_{-0.10}$
NGC 835	104/124	$1.40^{+0.25}_{-u}$	$23.46^{+0.09}_{-0.06}$	$23.22^{+0.16}_{-0.31}$	$0.05^{+0.34}_{-u}$	$0.40^{+0.20}_{-0.10}$	$0.04^{+0.01}_{-0.01}$	$-12.09^{+0.12}_{-0.58}$	$41.81^{+0.02}_{-0.08}$
NGC 1142	225/255	$1.48^{+0.16}_{-u}$	$24.20^{+0.08}_{-0.07}$	$23.49^{+0.15}_{-0.13}$	$0.05^{+0.28}_{-u}$	$0.45^{+0.14}_{-0.05}$	$0.36^{+0.17}_{-0.08}$	$-12.10^{+0.04}_{-0.16}$	$43.44^{+0.13}_{-0.11}$
NGC 2655	123/120	$2.12^{+0.23}_{-0.17}$	$23.51^{+0.08}_{-0.08}$	23.65^{+u}_{-u}	$0.15^{+0.64}_{-u}$	0.39^{+u}_{-u}	$0.22^{+0.02}_{-0.10}$	$-11.96^{+0.07}_{-2.54}$	$41.37^{+0.18}_{-0.16}$
NGC 3281	506/495	$1.77^{+0.12}_{-0.09}$	$24.30^{+0.06}_{-0.06}$	$25.50^{+u}_{-0.08}$	$0.55^{+0.13}_{-0.09}$	$0.52^{+0.12}_{-0.13}$	$0.68^{+0.31}_{-0.19}$	$-11.72^{+0.10}_{-0.23}$	$42.98^{+0.11}_{-0.10}$
NGC 4258	1577/1582	$1.92^{+0.08}_{-0.05}$	$22.94^{+0.02}_{-0.02}$	$23.49^{+0.26}_{-0.15}$	$0.95^{+u}_{-0.05}$	$0.90^{+0.05}_{-0.05}$	$0.21^{+0.03}_{-0.02}$	$-11.66^{+0.01}_{-0.03}$	$40.23^{+0.02}_{-0.01}$
NGC 4507	1383/1355	$1.63^{+0.05}_{-0.04}$	$23.87^{+0.02}_{-0.02}$	$22.90^{+0.16}_{-0.09}$	$0.51^{+0.11}_{-u}$	$0.66^{+0.12}_{-0.18}$	$1.49^{+0.32}_{-0.20}$	$-10.97^{+0.01}_{-0.01}$	$43.33^{+0.03}_{-0.04}$
NGC 4785	402/364	$1.96^{+0.15}_{-0.15}$	$23.70^{+0.04}_{-0.04}$	$24.43^{+0.37}_{-0.37}$	$0.63^{+0.22}_{-0.05}$	$0.70^{+u}_{-0.11}$	$0.21^{+0.12}_{-0.08}$	$-12.04^{+0.12}_{-0.07}$	$42.32^{+0.07}_{-0.12}$
NGC 4992	480/449	$1.50^{+0.06}_{-0.05}$	$23.46^{+0.03}_{-0.03}$	$24.00^{+0.04}_{-0.07}$	0.25^{+u}_{-u}	$1.00^{+u}_{-0.22}$	$0.18^{+0.05}_{-0.03}$	$-11.54^{+0.01}_{-0.14}$	$43.10^{+0.04}_{-0.06}$
NGC 5899	820/866	$1.99^{+0.03}_{-0.02}$	$23.08^{+0.01}_{-0.01}$	$24.79^{+0.13}_{-0.15}$	$0.95^{+u}_{-0.02}$	$0.95^{+0.01}_{-0.01}$	$0.43^{+0.01}_{-0.01}$	$-11.27^{+0.01}_{-0.02}$	$42.26^{+0.01}_{-0.01}$
NGC 6300	863/952	$1.90^{+0.05}_{-0.08}$	$23.21^{+0.03}_{-0.05}$	$24.40^{+0.16}_{-0.10}$	$0.73^{+0.13}_{-0.14}$	$0.81^{+0.13}_{-0.14}$	$0.11^{+0.02}_{-0.02}$	$-10.81^{+0.03}_{-0.01}$	$42.08^{+0.02}_{-0.03}$
NGC 7319	387/346	$1.71^{+0.09}_{-0.21}$	$23.81^{+0.04}_{-0.05}$	$25.50^{+u}_{-0.38}$	$0.69^{+0.20}_{-0.08}$	$0.70^{+0.05}_{-0.26}$	$0.27^{+0.10}_{-0.12}$	$-12.39^{+0.08}_{-0.15}$	$42.56^{+0.08}_{-0.10}$
PKS 2356-61	296/294	$1.90^{+0.04}_{-0.09}$	$23.23^{+0.03}_{-0.03}$	$25.50^{+u}_{-1.26}$	$0.76^{+0.17}_{-0.08}$	$0.76^{+0.07}_{-0.41}$	$0.21^{+0.02}_{-0.05}$	$-11.57^{+0.01}_{-0.06}$	$44.26^{+0.03}_{-0.03}$
SDSS J165315+234942	307/350	$1.50^{+0.09}_{-0.06}$	$23.20^{+0.06}_{-0.05}$	$22.95^{+1.33}_{-0.65}$	$0.95^{+u}_{-0.80}$	0.70^{+u}_{-u}	$0.08^{+0.02}_{-0.01}$	$-11.70^{+0.03}_{-0.07}$	$44.01^{+0.04}_{-0.05}$
VIIZw73*	93/96	$1.78^{+0.27}_{-0.26}$	$23.81^{+0.08}_{-0.09}$	–	–	–	$0.21^{+0.28}_{-0.12}$	$-12.17^{+0.05}_{-0.31}$	$43.49^{+0.20}_{-0.19}$
WISE J144850.99-400845.6*	1247/1099	$1.60^{+0.03}_{-0.04}$	$22.45^{+0.03}_{-0.03}$	–	–	–	$0.12^{+0.01}_{-0.01}$	$-11.28^{+0.01}_{-0.01}$	$44.74^{+0.01}_{-0.01}$

Notes. Column 2: Reduced χ^2, i.e., χ^2/ degree of freedom (d.o.f.). Column 4: Logarithm of line-of-sight column density in $\rm cm^{-2}$. If line-of-sight variability is found, the line-of-sight column density measured using *NuSTAR* data is reported. Column 5: Logarithm of average column density of the torus in $\rm cm^{-2}$. Column 6: Cosine of the inclination angle. $\cos(\theta) = 1$ is face-on and $\cos(\theta) = 0.05$ is edge-on. Column 7: Covering factor of the torus. Column 8: Normalization of the main cut-off power-law component at 1 keV in 10^{-2} photons $\rm keV^{-1}\,cm^{-2}\,s^{-1}$. Column 9: Logarithm of 2–10 keV flux of *NuSTAR* observation in $10^{-12}\,\rm erg\,cm^{-2}\,s^{-1}$. Column 10: Logarithm of 2–10 keV intrinsic luminosity of *NuSTAR* observation in $\rm erg\,s^{-1}$. The 1σ confidence level error is reported here. u is unconstrained when fitting the spectra. Sources labeled with asterisks are those fitted with only the line-of-sight component and the scattered component.

Table A.3. Best-fit results of the sources with *NuSTAR* (3–78 keV) data and *Chandra* (1–7 keV) data.

Source	χ^2/d.o.f.	Γ	$N_{\rm H,los}$	$N_{\rm H,tor}$	$\cos(\theta_{\rm inc})$	$c_{\rm f}$	Norm	$\rm Flux_{2-10}$	$L_{\rm int,2-10}$
2MASX J01073963-1139117	10/18	$1.82^{+0.50}_{-0.20}$	$24.48^{+u}_{-0.05}$	$23.47^{+0.29}_{-0.38}$	0.05^{+u}_{-u}	0.10^{+u}_{-u}	$1.13^{+4.69}_{-0.12}$	$-12.33^{+0.15}_{-u}$	$44.30^{+1.44}_{-0.93}$
3C 403	358/305	$2.11^{+0.09}_{-0.11}$	$23.65^{+0.03}_{-0.03}$	$24.76^{+u}_{-0.38}$	$0.56^{+0.25}_{-0.15}$	$0.60^{+0.28}_{-0.14}$	$0.67^{+0.19}_{-0.18}$	$-11.64^{+0.05}_{-0.03}$	$44.09^{+0.05}_{-0.05}$
4C +73.08	139/135	$1.40^{+0.12}_{-u}$	$23.53^{+0.04}_{-0.12}$	$22.93^{+0.21}_{-0.47}$	0.05^{+u}_{-u}	$0.70^{+u}_{-0.31}$	$0.08^{+0.00}_{-0.01}$	$-11.81^{+0.10}_{-0.31}$	$43.60^{+0.02}_{-0.05}$
CASG 218	201/209	$1.60^{+0.19}_{-0.14}$	$23.41^{+0.04}_{-0.08}$	$24.13^{+u}_{-1.48}$	0.35^{+u}_{-u}	$0.20^{+0.71}_{-u}$	$0.11^{+0.06}_{-0.04}$	$-11.73^{+0.04}_{-0.15}$	$43.55^{+0.08}_{-0.10}$
ESO 119-8*	91/106	$1.66^{+0.18}_{-0.17}$	$23.17^{+0.09}_{-0.09}$	–	–	–	$0.03^{+0.02}_{-0.01}$	$-12.19^{+0.03}_{-0.07}$	$42.25^{+0.08}_{-0.07}$
ESO 500-34	115/120	$2.34^{+0.25}_{-0.43}$	$23.67^{+0.09}_{-0.05}$	$24.17^{+u}_{-0.45}$	$0.15^{+0.71}_{-u}$	$0.88^{+u}_{-0.68}$	$0.62^{+0.72}_{-0.42}$	$-11.92^{+0.15}_{-0.56}$	$42.52^{+0.17}_{-0.27}$
IC 5063	732/742	$1.77^{+0.08}_{-0.07}$	$23.36^{+0.02}_{-0.02}$	$24.31^{+0.24}_{-0.21}$	$0.48^{+0.16}_{-0.11}$	$0.53^{+0.22}_{-0.15}$	$0.71^{+0.14}_{-0.12}$	$-11.06^{+0.02}_{-0.02}$	$42.87^{+0.03}_{-0.03}$
LEDA 15023	78/77	$1.91^{+0.25}_{-0.25}$	$23.97^{+0.08}_{-0.18}$	$23.18^{+0.18}_{-0.28}$	$0.05^{+0.12}_{-u}$	$0.18^{+0.12}_{-u}$	$0.88^{+1.23}_{-0.51}$	$-11.86^{+0.03}_{-0.52}$	$44.09^{+0.10}_{-0.11}$
NGC 4102	297/300	$1.74^{+0.12}_{-0.08}$	$23.87^{+0.04}_{-0.03}$	$25.15^{+u}_{-0.68}$	$0.53^{+0.16}_{-0.24}$	$0.61^{+0.31}_{-0.22}$	$0.46^{+0.22}_{-0.12}$	$-11.84^{+0.31}_{-0.04}$	$41.49^{+0.09}_{-0.06}$
NGC 4388	953/871	$1.64^{+0.05}_{-0.08}$	$23.43^{+0.02}_{-0.02}$	$24.00^{+0.07}_{-0.20}$	$0.60^{+0.15}_{-0.04}$	$0.60^{+0.16}_{-0.05}$	$0.49^{+0.06}_{-0.09}$	$-11.14^{+0.01}_{-0.02}$	$42.52^{+0.03}_{-0.03}$
NGC 4939	228/234	$1.69^{+0.19}_{-0.15}$	$23.82^{+0.09}_{-0.08}$	$23.02^{+0.13}_{-0.14}$	$0.05^{+0.45}_{-u}$	$0.57^{+0.13}_{-0.14}$	$0.31^{+0.30}_{-0.13}$	$-11.80^{+0.01}_{-0.15}$	$42.49^{+0.16}_{-0.13}$
NGC 4941	106/111	$1.40^{+0.31}_{-u}$	$23.98^{+0.30}_{-0.20}$	$24.50^{+0.44}_{-0.68}$	$0.65^{+u}_{-0.20}$	$0.40^{+0.43}_{-0.23}$	$0.06^{+0.01}_{-0.03}$	$-12.28^{+0.06}_{-u}$	$41.04^{+0.43}_{-0.46}$
NGC 5283	343/302	$1.81^{+0.16}_{-0.17}$	$23.04^{+0.11}_{-0.09}$	$24.39^{+u}_{-0.80}$	$0.60^{+u}_{-0.19}$	$0.50^{+u}_{-0.32}$	$0.13^{+0.05}_{-0.04}$	$-11.62^{+0.01}_{-0.11}$	$42.02^{+0.06}_{-0.06}$
NGC 5728	417/446	$1.80^{+0.02}_{-0.10}$	$24.09^{+0.03}_{-0.01}$	$25.21^{+u}_{-0.61}$	$0.52^{+0.21}_{-0.01}$	$0.59^{+0.00}_{-0.11}$	$1.80^{+0.92}_{-0.03}$	$-11.78^{+0.52}_{-0.15}$	$43.08^{+0.09}_{-0.04}$
NGC 5972	177/188	$1.75^{+0.36}_{-0.21}$	$23.79^{+0.13}_{-0.07}$	$24.34^{+u}_{-0.18}$	$0.85^{+0.03}_{-0.33}$	$0.90^{+u}_{-0.32}$	$0.08^{+0.22}_{-0.03}$	$-12.35^{+0.10}_{-u}$	$42.79^{+0.07}_{-0.09}$
SDSS J135429.05+132757.2*	113/149	$1.61^{+0.16}_{-0.15}$	$23.45^{+0.09}_{-0.11}$	–	–	–	$0.11^{+0.07}_{-0.04}$	$-11.83^{+0.01}_{-0.07}$	$43.67^{+0.11}_{-0.10}$
UGC 3995B	234/258	$1.61^{+0.05}_{-0.09}$	$23.48^{+0.04}_{-0.02}$	$24.25^{+0.08}_{-0.16}$	$0.87^{+0.05}_{-u}$	$0.94^{+u}_{-0.18}$	$0.15^{+0.07}_{-0.03}$	$-11.68^{+0.02}_{-0.19}$	$42.58^{+0.03}_{-0.15}$
UGC 4211	295/304	$1.77^{+0.11}_{-0.09}$	$22.95^{+0.05}_{-0.05}$	$23.43^{+0.41}_{-0.58}$	0.05^{+u}_{-u}	$0.70^{+u}_{-0.60}$	$0.15^{+0.07}_{-0.03}$	$-11.38^{+0.01}_{-0.13}$	$43.28^{+0.04}_{-0.05}$
Was49b*	215/171	$1.49^{+0.13}_{-0.12}$	$23.30^{+0.11}_{-0.10}$	–	–	–	$0.08^{+0.04}_{-0.02}$	$-11.69^{+0.07}_{-0.06}$	$43.65^{+0.10}_{-0.09}$

Table A.4. Best-fit results of the sources with *NuSTAR* (3–78 keV) data and *Swift*-XRT (1–10 keV) data.

Source	Cstat/d.o.f.	Γ	$N_{\rm H,los}$	$N_{\rm H,tor}$	$\cos(\theta_{\rm inc})$	$c_{\rm f}$	Norm	$\rm Flux_{2-10}$	$L_{\rm int,2-10}$
2MASX J00502684+8229000	128/160	$2.02^{+0.21}_{-0.22}$	$23.21^{+0.19}_{-0.17}$	$24.15^{+0.17}_{-0.37}$	0.95^{+u}_{-u}	$0.98^{+u}_{-0.17}$	$0.17^{+0.15}_{-0.07}$	$-11.72^{+0.05}_{-0.19}$	$43.13^{+0.48}_{-0.27}$
2MASX J09235371−3141305*	183/148	$1.37^{+0.14}_{-0.13}$	$23.67^{+0.07}_{-0.08}$	–	–	–	$0.13^{+0.08}_{-0.05}$	$-11.81^{+0.02}_{-0.06}$	$43.56^{+0.11}_{-0.11}$
2MASX J11140245+2023140*	106/109	$1.53^{+0.27}_{-0.25}$	$23.70^{+0.11}_{-0.13}$	–	–	–	$0.08^{+0.12}_{-0.05}$	$-12.18^{+0.01}_{-0.68}$	$42.83^{+0.21}_{-0.19}$
ESO 21-4*	215/180	$1.57^{+0.15}_{-0.14}$	$23.43^{+0.10}_{-0.10}$	–	–	–	$0.12^{+0.08}_{-0.04}$	$-11.75^{+0.02}_{-0.05}$	$42.11^{+0.11}_{-0.10}$
ESO 121-28	289/303	$2.07^{+0.08}_{-0.08}$	$23.40^{+0.05}_{-0.08}$	$24.25^{+0.04}_{-0.19}$	0.35^{+u}_{-u}	$1.00^{+u}_{-0.29}$	$0.53^{+0.15}_{-0.20}$	$-11.47^{+0.02}_{-0.08}$	$43.67^{+0.05}_{-0.10}$
ESO 231-26	296/309	$1.74^{+0.18}_{-0.14}$	$23.37^{+0.08}_{-0.07}$	$24.52^{+u}_{-0.49}$	$0.26^{+0.34}_{-u}$	$0.40^{+0.37}_{-u}$	$0.27^{+0.15}_{-0.12}$	$-11.50^{+0.04}_{-0.06}$	$43.96^{+0.09}_{-0.10}$
ESO 505-30	292/299	$1.84^{+0.05}_{-0.14}$	$23.10^{+0.08}_{-0.09}$	$24.20^{+0.20}_{-0.33}$	$0.05^{+0.53}_{-u}$	$0.50^{+0.43}_{-0.19}$	$0.19^{+0.04}_{-0.04}$	$-11.41^{+0.05}_{-0.05}$	$43.48^{+0.06}_{-0.06}$
ESO 553-43*	488/493	$1.63^{+0.05}_{-0.05}$	$23.18^{+0.06}_{-0.04}$	–	–	–	$0.34^{+0.05}_{-0.05}$	$-11.19^{+0.01}_{-0.01}$	$43.42^{+0.03}_{-0.03}$
IC 1657	161/143	$1.58^{+0.36}_{-u}$	$23.53^{+0.21}_{-0.21}$	$24.11^{+u}_{-1.09}$	$0.67^{+0.24}_{-0.36}$	$0.70^{+u}_{-0.58}$	$0.07^{+0.06}_{-0.03}$	$-11.94^{+0.04}_{-u}$	$42.00^{+0.28}_{-0.19}$
IC 4709	353/326	$1.81^{+0.16}_{-0.15}$	$23.38^{+0.02}_{-0.12}$	$24.16^{+0.08}_{-0.22}$	0.95^{+u}_{-u}	$0.98^{+u}_{-0.06}$	$0.32^{+0.21}_{-0.11}$	$-11.42^{+0.04}_{-0.09}$	$42.77^{+0.07}_{-0.05}$
IRAS 05581+0006	201/199	$1.47^{+0.22}_{-u}$	$23.32^{+0.11}_{-0.12}$	$24.00^{+u}_{-0.32}$	$0.35^{+0.44}_{-u}$	0.50^{+u}_{-u}	$0.08^{+0.05}_{-0.02}$	$-11.72^{+0.04}_{-0.51}$	$44.15^{+0.12}_{-0.08}$
IRAS 20247−7542	446/401	$1.62^{+0.07}_{-0.11}$	$23.02^{+0.07}_{-0.08}$	$24.03^{+0.17}_{-0.16}$	$0.90^{+u}_{-0.41}$	$0.35^{+0.54}_{-u}$	$0.11^{+0.02}_{-0.02}$	$-11.49^{+0.05}_{-0.04}$	$44.23^{+0.04}_{-0.05}$
LEDA 2265450*	222/224	$1.66^{+0.11}_{-0.11}$	$23.46^{+0.06}_{-0.06}$	–	–	–	$0.22^{+0.09}_{-0.06}$	$-11.62^{+0.01}_{-0.03}$	$43.18^{+0.03}_{-0.02}$
LEDA 46599	299/263	$1.88^{+0.21}_{-0.26}$	$23.40^{+0.08}_{-0.12}$	$24.82^{+u}_{-2.12}$	$0.91^{+u}_{-0.38}$	$0.43^{+0.32}_{-u}$	$0.26^{+0.10}_{-0.07}$	$-11.54^{+0.01}_{-0.11}$	$43.35^{+0.11}_{-0.11}$
LEDA 259433	190/196	$1.80^{+0.18}_{-0.01}$	$23.07^{+0.15}_{-0.21}$	$24.10^{+0.25}_{-0.30}$	0.05^{+u}_{-u}	$1.00^{+u}_{-0.17}$	$0.12^{+0.08}_{-0.05}$	$-11.65^{+0.01}_{-0.17}$	$43.93^{+0.09}_{-0.08}$
LEDA 549777*	196/187	$1.58^{+0.10}_{-0.10}$	$23.11^{+0.07}_{-0.11}$	–	–	–	$0.07^{+0.03}_{-0.01}$	$-11.75^{+0.01}_{-0.03}$	$43.39^{+0.06}_{-0.05}$
MCG+11-11-32	117/133	$1.88^{+0.09}_{-0.10}$	$23.11^{+0.09}_{-0.07}$	$24.34^{+0.25}_{-0.19}$	0.65^{+u}_{-u}	$1.00^{+u}_{-0.32}$	$0.50^{+0.16}_{-0.12}$	$-11.16^{+0.03}_{-0.08}$	$43.67^{+0.04}_{-0.07}$
MCG−02-15-004	127/120	$2.14^{+0.42}_{-0.07}$	$23.74^{+0.05}_{-0.11}$	$24.25^{+0.17}_{-0.22}$	0.87^{+u}_{-u}	$0.98^{+u}_{-0.50}$	$0.46^{+0.08}_{-0.02}$	$-11.77^{+0.09}_{-u}$	$43.30^{+0.15}_{-0.09}$
NGC 1229	115/135	$1.45^{+0.34}_{-u}$	$23.32^{+0.14}_{-0.09}$	$24.31^{+u}_{-0.28}$	$0.86^{+u}_{-0.37}$	$0.80^{+u}_{-0.53}$	$0.03^{+0.08}_{-0.00}$	$-12.11^{+0.03}_{-u}$	$42.77^{+0.20}_{-0.09}$
NGC 4500	40/30	$1.54^{+0.58}_{-u}$	$23.36^{+0.21}_{-0.46}$	$23.52^{+0.78}_{-u}$	0.95^{+u}_{-u}	0.71^{+u}_{-u}	$0.01^{+0.02}_{-0.01}$	$-12.41^{+0.03}_{-u}$	$41.24^{+0.58}_{-0.18}$
NGC 6232	14/14	$1.40^{+0.59}_{-u}$	$23.72^{+0.51}_{-0.08}$	$24.75^{+u}_{-0.81}$	0.55^{+u}_{-u}	$0.90^{+u}_{-0.74}$	$0.01^{+0.00}_{-0.01}$	$-12.68^{+0.69}_{-u}$	$41.56^{+0.09}_{-0.60}$
UGC 3157	121/134	$2.21^{+0.34}_{-0.26}$	$23.85^{+0.07}_{-0.04}$	$24.84^{+0.10}_{-0.29}$	$0.91^{+u}_{-0.06}$	$1.00^{+u}_{-0.32}$	$0.82^{+1.44}_{-0.03}$	$-11.93^{+0.07}_{-u}$	$42.91^{+0.16}_{-0.02}$
UGC 3752	149/129	$2.03^{+0.01}_{-0.02}$	$24.00^{+0.01}_{-0.03}$	$24.58^{+0.09}_{-0.10}$	$0.90^{+0.02}_{-0.01}$	$0.91^{+0.08}_{-0.38}$	$0.43^{+0.02}_{-0.02}$	$-12.22^{+0.05}_{-u}$	$42.77^{+0.01}_{-0.02}$
Z319-7*	133/113	$1.39^{+0.17}_{-0.15}$	$23.18^{+0.14}_{-0.23}$	–	–	–	$0.05^{+0.03}_{-0.02}$	$-11.82^{+0.03}_{-0.09}$	$43.14^{+0.11}_{-0.09}$
Z333-49*	213/192	$1.67^{+0.13}_{-0.12}$	$23.20^{+0.10}_{-0.09}$	–	–	–	$0.10^{+0.04}_{-0.03}$	$-11.77^{+0.02}_{-0.03}$	$43.02^{+0.07}_{-0.07}$
Z367-9	196/203	$1.66^{+0.13}_{-0.16}$	$23.11^{+0.12}_{-0.21}$	$23.75^{+0.13}_{-0.24}$	0.05^{+u}_{-u}	0.59^{+u}_{-u}	$0.04^{+0.02}_{-0.01}$	$-11.89^{+0.01}_{-0.14}$	$42.41^{+0.05}_{-0.08}$

Notes. Column 2: Reduced C statistic.

Table A.5. Reanalysis best-fit results of the CT-AGN in Marchesi et al. (2019).

Source	Statistics	Γ	$N_{\rm H,los}$	$N_{\rm H,tor}$	$\cos(\theta_{\rm inc})$	$c_{\rm f}$	Norm	$\rm Flux_{2-10}$	$L_{\rm int,2-10}$
CGCG 164-19	38/37	$1.67^{+0.34}_{-u}$	$23.77^{+0.18}_{-0.16}$	$24.56^{+u}_{-0.38}$	0.89^{+u}_{-u}	$0.90^{+u}_{-0.73}$	$0.05^{+0.10}_{-0.05}$	$-12.36^{+0.33}_{-u}$	$42.61^{+0.17}_{-0.34}$
ESO 005-G004	59/47	$1.90^{+u}_{-0.40}$	$24.67^{+0.37}_{-0.37}$	$24.15^{+0.28}_{-0.29}$	$0.78^{+0.15}_{-0.45}$	$0.79^{+0.14}_{-0.47}$	$0.32^{+2.78}_{-0.32}$	$-12.27^{+0.06}_{-u}$	$41.92^{+0.49}_{-0.23}$
ESO 201-004	99/92	$1.97^{+0.28}_{-0.35}$	$24.34^{+0.09}_{-0.14}$	$23.28^{+0.08}_{-0.12}$	$0.05^{+0.18}_{-u}$	$0.20^{+0.26}_{-u}$	$0.99^{+1.23}_{-0.63}$	$-12.38^{+0.03}_{-u}$	$43.90^{+0.45}_{-0.32}$
MCG +08-03-018	125/131	$1.98^{+0.09}_{-0.12}$	$23.97^{+0.09}_{-0.09}$	$23.00^{+0.13}_{-0.23}$	0.55^{+u}_{-u}	$1.00^{+u}_{-0.64}$	$0.49^{+0.22}_{-0.30}$	$-11.89^{+0.07}_{-0.13}$	$43.08^{+0.10}_{-0.29}$
NGC 424	422/335	$2.12^{+0.04}_{-0.04}$	$24.51^{+0.02}_{-0.02}$	$23.81^{+0.05}_{-0.07}$	$0.06^{+0.01}_{-u}$	$0.10^{+0.01}_{-u}$	$5.27^{+1.59}_{-2.76}$	$-12.00^{+0.12}_{-0.64}$	$43.54^{+0.06}_{-0.06}$
NGC 1194	275/267	$1.91^{+0.11}_{-0.18}$	$23.99^{+0.05}_{-0.07}$	$24.75^{+u}_{-0.37}$	$0.86^{+0.07}_{-0.16}$	$0.85^{+0.06}_{-0.20}$	$0.39^{+0.16}_{-0.20}$	$-11.97^{+0.04}_{-u}$	$42.71^{+0.07}_{-0.09}$
NGC 3079	111/111	$2.04^{+0.20}_{-0.22}$	$24.75^{+u}_{-0.37}$	$23.81^{+0.05}_{-0.07}$	$0.15^{+0.18}_{-0.10}$	$0.23^{+0.20}_{-0.04}$	$4.07^{+8.00}_{-4.07}$	$-12.28^{+0.44}_{-u}$	$42.71^{+0.45}_{-1.10}$
NGC 3393	120/110	$1.60^{+0.20}_{-0.17}$	$24.27^{+0.24}_{-0.13}$	$24.21^{+0.05}_{-0.16}$	$0.05^{+0.64}_{-u}$	$0.55^{+0.37}_{-0.42}$	$0.43^{+0.40}_{-0.20}$	$-12.43^{+0.18}_{-2.51}$	$42.85^{+0.80}_{-0.67}$
NGC 4945	1144/1167	$1.92^{+0.02}_{-0.02}$	$24.55^{+0.01}_{-0.01}$	$24.65^{+0.04}_{-0.03}$	$0.05^{+0.01}_{-u}$	$0.12^{+0.01}_{-0.01}$	$76.86^{+0.76}_{-0.76}$	$-11.54^{+0.10}_{-0.15}$	$43.24^{+0.01}_{-0.01}$
NGC 5100	178/171	$1.69^{+0.04}_{-0.13}$	$23.29^{+0.02}_{-0.09}$	$25.50^{+u}_{-0.23}$	$0.95^{+u}_{-0.52}$	$0.25^{+0.05}_{-0.13}$	$0.17^{+0.06}_{-0.01}$	$-11.53^{+0.23}_{-0.09}$	$43.21^{+0.06}_{-0.04}$
NGC 5643	191/173	$1.63^{+0.16}_{-0.14}$	>24.24	$24.07^{+0.06}_{-0.20}$	$0.95^{+u}_{-0.59}$	$0.80^{+0.11}_{-0.24}$	$0.12^{+0.03}_{-0.02}$	$-12.13^{+0.11}_{-2.04}$	$41.35^{+0.06}_{-0.02}$
NGC 5728	417/446	$1.80^{+0.02}_{-0.10}$	$24.09^{+0.03}_{-0.01}$	$25.21^{+u}_{-0.61}$	$0.52^{+0.21}_{-0.01}$	$0.59^{+0.00}_{-0.11}$	$1.80^{+0.92}_{-0.03}$	$-11.78^{+0.52}_{-0.15}$	$43.08^{+0.09}_{-0.04}$
NGC 6240	494/476	$1.69^{+0.08}_{-0.05}$	$24.08^{+0.05}_{-0.05}$	$24.16^{+0.20}_{-0.04}$	$0.25^{+0.21}_{-u}$	$0.50^{+0.21}_{-0.21}$	$0.73^{+0.26}_{-0.15}$	$-11.64^{+0.23}_{-0.14}$	$43.67^{+0.15}_{-0.12}$
NGC 7130	81/81	$1.71^{+0.43}_{-u}$	>24.16	$24.61^{+u}_{-0.32}$	$0.28^{+0.62}_{-0.17}$	$0.37^{+0.61}_{-0.23}$	$0.37^{+1.63}_{-0.33}$	$-12.67^{+0.06}_{-1.31}$	$42.93^{+0.66}_{-u}$
NGC 7212	110/106	$2.22^{+0.04}_{-0.29}$	$24.28^{+0.12}_{-0.11}$	$23.86^{+0.99}_{-0.19}$	$0.15^{+0.02}_{-0.06}$	$0.10^{+0.33}_{-u}$	$2.36^{+3.83}_{-0.61}$	$-12.25^{+0.01}_{-1.97}$	$43.78^{+0.12}_{-0.24}$
NGC 7479	195/165	$2.29^{+0.26}_{-0.25}$	$24.76^{+0.08}_{-0.07}$	$25.08^{+u}_{-0.16}$	$0.15^{+0.01}_{-0.01}$	$0.29^{+0.01}_{-0.01}$	$46.80^{+49.59}_{-24.72}$	$-12.62^{+0.19}_{-2.37}$	$44.18^{+0.17}_{-0.22}$
NGC 7582	1708/1544	$1.64^{+0.02}_{-0.03}$	$24.23^{+0.02}_{-0.04}$	$23.29^{+0.02}_{-0.06}$	$0.25^{+0.07}_{-0.06}$	$0.90^{+u}_{-0.11}$	$0.76^{+0.01}_{-0.07}$	$-11.30^{+0.06}_{-0.06}$	$42.57^{+0.01}_{-0.01}$

Notes. Column 2: χ^2/d.o.f. for sources using *XMM-Newton* and *Chandra* data and cstat/d.o.f. for sources using *Swift*-XRT data.

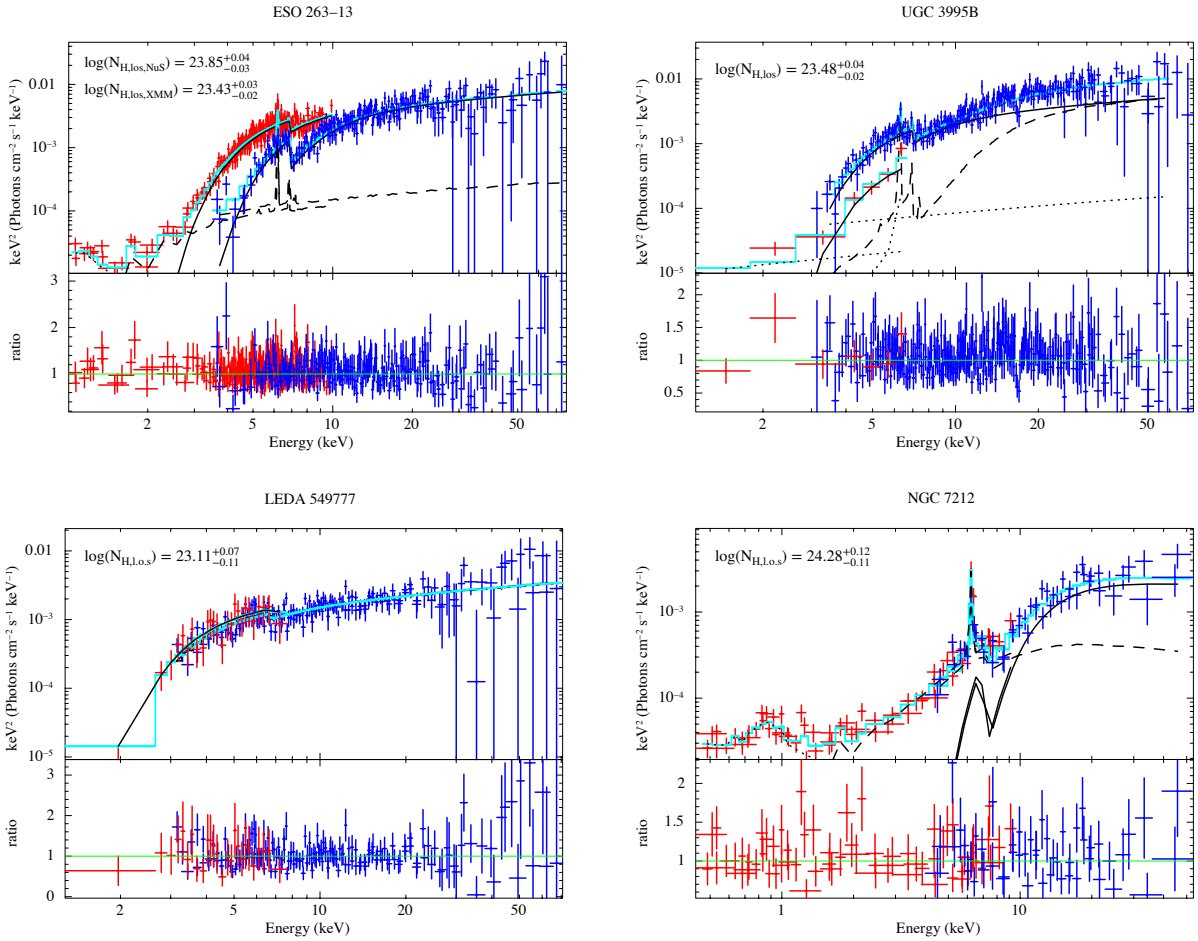

Fig. A.1. Spectra and ratio (between the data and model predictions) of ESO 263-13 (*XMM-Newton*+*NuSTAR*), UCG 3995B (*Chandra*+*NuSTAR*), LEDA 549777 (*Swift*-XRT+*NuSTAR*) and NGC 7212 (in M19 sample). *NuSTAR* and soft X-ray data are plotted in blue and red, respectively. The total best-fit model predictions and different components of the models of are plotted in cyan and black, respectively. The reprocessed component, line-of-sight component, and scattered (and Mekal) component are plotted in dashed, solid, and dotted lines, respectively. Significant flux variabilities are found in ESO 263-13 and UGC 3995B.

Appendix B: Variability analysis

Table B.1. Best-fit results of sources with flux variabilities in our sample and M19 sample.

Source	$C_{\rm soft/NuS}$	$N_{\rm H,los,NuS}$	$N_{\rm H,los,soft}$	$\Delta N_{\rm H,los}$	ΔT
2MASX J06411806+3249313	$0.75^{+0.12}_{-0.10}$	$23.09^{+0.08}_{-0.10}$	$23.27^{+0.06}_{-0.07}$	$0.18^{+0.12}_{-0.11}$	12.80
3C 105*	$2.63^{+0.23}_{-0.19}$	$23.65^{+0.10}_{-0.03}$	–	–	8.34
3C 445	$1.43^{+0.09}_{-0.08}$	$23.08^{+0.05}_{-0.07}$	$23.21^{+0.02}_{-0.04}$	$0.13^{+0.07}_{-0.06}$	14.44
3C 452	$1.30^{+0.11}_{-0.02}$	$23.59^{+0.03}_{-0.01}$	$23.82^{+0.06}_{-0.01}$	$0.23^{+0.06}_{-0.03}$	8.42
4C +29.30	1^{f}	$23.50^{+0.04}_{-0.06}$	$23.68^{+0.03}_{-0.03}$	$0.18^{+0.07}_{-0.05}$	5.58
4C +73.08	1^{f}	$23.53^{+0.04}_{-0.12}$	$23.70^{+0.03}_{-0.05}$	$0.17^{+0.12}_{-0.06}$	7.40
ESO 21-4*	1^{f}	$23.43^{+0.10}_{-0.10}$	$23.67^{+0.13}_{-0.13}$	$0.24^{+0.16}_{-0.16}$	4.63
ESO 103-35	$1.33^{+0.04}_{-0.03}$	$23.25^{+0.02}_{-0.02}$	$23.28^{+0.01}_{-0.01}$	$0.03^{+0.02}_{-0.02}$	15.58
ESO 119-8*	$2.01^{+0.34}_{-0.30}$	$23.17^{+0.09}_{-0.09}$	–	–	0.03
ESO 263-13	$0.81^{+0.08}_{-0.08}$	$23.85^{+0.04}_{-0.03}$	$23.43^{+0.03}_{-0.02}$	$0.42^{+0.04}_{-0.04}$	1.67
ESO 383-18	$1.43^{+0.06}_{-0.02}$	$23.28^{+0.03}_{-0.02}$	$23.32^{+0.01}_{-0.03}$	$0.04^{+0.02}_{-0.04}$	10.03
ESO 439-G009	1^{f}	$23.58^{+0.09}_{-0.09}$	$23.69^{+0.07}_{-0.05}$	$0.11^{+0.11}_{-0.10}$	0.54
ESO 553-43*	$0.63^{+0.08}_{-0.07}$	$23.18^{+0.05}_{-0.04}$	–	–	5.75
Fairall 272	$0.83^{+0.09}_{-0.09}$	$23.23^{+0.05}_{-0.05}$	$23.51^{+0.03}_{-0.06}$	$0.27^{+0.06}_{-0.08}$	6.24
IC 1657	$3.11^{+1.06}_{-0.83}$	$23.53^{+0.21}_{-0.21}$	–	–	8.20
IC 4518A	$0.81^{+0.15}_{-0.13}$	$23.11^{+0.12}_{-0.16}$	$23.36^{+0.07}_{-0.04}$	$0.25^{+0.17}_{-0.13}$	6.99
IC 4709	$2.43^{+0.49}_{-0.43}$	$23.38^{+0.02}_{-0.12}$	–	–	6.74
IRAS 16288+3929	1^{f}	$23.88^{+0.06}_{-0.10}$	$23.75^{+0.06}_{-0.11}$	$0.13^{+0.13}_{-0.12}$	1.03
LEDA 259433	1^{f}	$23.05^{+0.17}_{-0.24}$	$23.34^{+0.12}_{-0.28}$	$0.29^{+0.27}_{-0.29}$	1.54
LEDA 2816387*	1^{f}	$23.76^{+0.05}_{-0.07}$	$23.87^{+0.04}_{-0.04}$	$0.11^{+0.08}_{-0.06}$	1.54
LEDA 511869	$2.17^{+0.21}_{-0.25}$	$23.88^{+0.07}_{-0.03}$	–	–	1.71
MCG -01-05-047	$1.23^{+0.16}_{-0.15}$	$23.33^{+0.09}_{-0.09}$	$23.23^{+0.03}_{-0.04}$	$0.10^{+0.10}_{-0.09}$	3.35
MCG +11-11-32	$0.68^{+0.14}_{-0.12}$	$23.11^{+0.09}_{-0.07}$	–	–	0.18
Mrk 348	$0.93^{+0.02}_{-0.03}$	$22.92^{+0.03}_{-0.03}$	$23.14^{+0.01}_{-0.01}$	$0.22^{+0.03}_{-0.03}$	13.28
Mrk 417	1^{f}	$23.53^{+0.06}_{-0.07}$	$23.81^{+0.04}_{-0.05}$	$0.28^{+0.07}_{-0.08}$	10.68
Mrk 477	1^{f}	$23.30^{+0.06}_{-0.07}$	$23.70^{+0.03}_{-0.04}$	$0.40^{+0.07}_{-0.07}$	3.82
Mrk 1210	$1.30^{+0.05}_{-0.05}$	$23.30^{+0.04}_{-0.02}$	–	–	11.42
NGC 454E	1^{f}	$23.86^{+0.04}_{-0.04}$	$23.37^{+0.04}_{-0.03}$	$0.49^{+0.05}_{-0.06}$	6.27
NGC 612	$1.49^{+0.15}_{-0.08}$	$23.95^{+0.05}_{-0.04}$	–	–	6.22
NGC 788	$1.59^{+0.10}_{-0.10}$	$23.79^{+0.04}_{-0.05}$	–	–	3.04
NGC 835	1^{f}	$23.46^{+0.09}_{-0.06}$	$24.06^{+0.14}_{-0.08}$	$0.60^{+0.17}_{-0.12}$	15.64
NGC 1142	$1.43^{+0.39}_{-0.37}$	$24.20^{+0.08}_{-0.07}$	$23.75^{+0.07}_{-0.05}$	$0.45^{+0.09}_{-0.10}$	11.71
NGC 3281	$0.65^{+0.07}_{-0.07}$	$24.30^{+0.06}_{-0.06}$	$23.90^{+0.05}_{-0.04}$	$0.40^{+0.07}_{-0.08}$	5.05
NGC 4388	$1.89^{+0.05}_{-0.04}$	$23.43^{+0.02}_{-0.02}$	–	–	5.70
NGC 4507	$0.68^{+0.01}_{-0.00}$	$23.88^{+0.01}_{-0.01}$	–	–	4.85
NGC 4939	1^{f}	$23.82^{+0.09}_{-0.08}$	$23.69^{+0.09}_{-0.08}$	$0.13^{+0.12}_{-0.12}$	6.69
NGC 4941	1^{f}	$23.98^{+0.30}_{-0.20}$	$23.58^{+0.32}_{-0.24}$	$0.40^{+0.38}_{-0.38}$	6.69
NGC 4992	$1.12^{+0.11}_{-0.10}$	$23.46^{+0.03}_{-0.03}$	$23.67^{+0.03}_{-0.01}$	$0.21^{+0.04}_{-0.03}$	10.58
NGC 5283	$0.64^{+0.07}_{-0.07}$	$23.04^{+0.11}_{-0.09}$	–	–	14.98
NGC 6300	$0.085^{+0.008}_{-0.006}$	$23.21^{+0.03}_{-0.05}$	$23.34^{+0.03}_{-0.01}$	$0.13^{+0.06}_{-0.03}$	15.48
NGC 7319	$3.33^{+0.24}_{-0.20}$	$23.81^{+0.04}_{-0.05}$	–	–	15.80
UGC 3995B	$0.30^{+0.04}_{-0.04}$	$23.48^{+0.04}_{-0.02}$	–	–	0.75
Z367-9	$4.03^{+0.50}_{-0.46}$	$23.11^{+0.12}_{-0.21}$	–	–	7.56
CGCG 164-19	1^{f}	$23.77^{+0.18}_{-0.16}$	$23.41^{+0.27}_{-0.35}$	$0.36^{+0.39}_{-0.31}$	2.80
ESO 201-004	1^{f}	$24.34^{+0.09}_{-0.14}$	$24.19^{+0.08}_{-0.14}$	$0.15^{+0.17}_{-0.15}$	7.07
NGC 7479	$0.78^{+0.14}_{-0.11}$	$24.76^{+0.08}_{-0.07}$	$24.56^{+0.04}_{-0.06}$	$0.20^{+0.10}_{-0.08}$	2.05
NGC 7582	$0.56^{+0.06}_{-0.01}$	$24.23^{+0.02}_{-0.04}$	$23.58^{+0.02}_{-0.01}$	$0.65^{+0.02}_{-0.04}$	3.66

Notes. Column 2: Cross-calibration factor between the soft X-ray spectra and *NuSTAR* spectra. Column 3: Logarithm of "line-of-sight" column density of *NuSTAR* observation in $\rm cm^{-2}$. Column 4: Logarithm of "line-of-sight" column density of soft X-ray observation in $\rm cm^{-2}$. Column 5: Absolute difference between $N_{\rm H,los,NuS}$ and $N_{\rm H,los,soft}$. Column 6: Time interval between the *NuSTAR* observation and the soft X-ray observation in years. Sources labeled with asterisks are those fitted with only the line-of-sight component and the scattered component.

To properly characterize the spectra of the sources observed with flux variation between the *NuSTAR* observations and soft X-ray observations (2–10 keV flux variation >20 percent), we fit them three times: 1. First we allow the cross-calibration factor between the soft X-rays spectra and *NuSTAR* spectra, $C_{\rm soft/NuS}$, free to vary, assuming the flux variability is caused by the intrinsic emission variation. The sources whose flux variabilities are thought to be caused by intrinsic emission variations are those with $C_{\rm soft/NuS}$ different from unity at 90% confidence level. 2. Second, we fix $C_{\rm soft/NuS} = 1$, and disentangling the line-of-sight column densities of the soft-X-ray observations, $N_{\rm H,los,soft}$ and *NuSTAR* observations, $N_{\rm H,los,NuS}$, assuming the flux variability is caused by $N_{\rm H,los}$ variations. The sources whose flux variabilities are caused by $N_{\rm H,los}$ variations are those whose $N_{\rm H,los,NuS}$ are different from their $N_{\rm H,los,soft}$ at 90% confidence level. 3. Finally, we allow $C_{\rm soft/NuS}$ free to vary and disentangling the $N_{\rm H,los,soft}$ and $N_{\rm H,los,NuS}$, assuming the flux variability is caused by both the intrinsic emission and $N_{\rm H,los}$ variations. If the improvement in the fit is >90% confidence level using the `ftest` in `XSPEC` with respect to the previous two scenarios the first two scenarios, we assume that the flux variability of this source is the result of both intrinsic emission and $N_{\rm H,los}$ variations. Otherwise, the cause of the flux variation of this source is determined by comparing the reduced statistics (χ^2/d.o.f or cstat/d.o.f) of the best-fit of the first two scenarios. For sources whose flux variabilities are caused by the $N_{\rm H,los}$ variations only, we fix their cross-calibration factors at $C_{\rm soft/NuS} = 1$ to better constrain the other parameters. Here, we assume a consistent reprocessed component and scattered component between different observing epochs, considering that the global structure and properties of the obscuring torus is stable over a timescale of a few years. We summarize the best-fit results of the sources with observed flux variability (including four variable sources from M19 sample) in Table B.1.